

Document NWPSAF-MO-TR-031


Version 1.2

20/12/2016

# A visible/infrared multiple-scattering model for RTTOV

James Hocking

Met Office  
Fitzroy Road, Exeter, EX1 3PB, United Kingdom

The EUMETSAT Network of Satellite Application Facilities	 <b>NWP SAF</b> Numerical Weather Prediction	<b>A visible/infrared multiple-scattering model for RTTOV</b>	Doc ID : NWPSAF-MO-TR-031 Version : 1.2 Date : 20/12/2016
---	--	---	---

# A visible/infrared multiple-scattering model for RTTOV

**James Hocking**

Met Office, Fitzroy Road, Exeter, EX1 3PB, United Kingdom

This documentation was developed within the context of the EUMETSAT Satellite Application Facility on Numerical Weather Prediction (NWP SAF), under the Cooperation Agreement dated 29 June 2011, between EUMETSAT and the Met Office, UK, by one or more partners within the NWP SAF. The partners in the NWP SAF are the Met Office, ECMWF, KNMI and Météo France.

Copyright 2016, EUMETSAT, All Rights Reserved.

Change record			
Version	Date	Author / changed by	Remarks
1.0	14/12/15	James Hocking	
1.1	28/09/16	James Hocking	Updated for RTTOV v12 release
1.2	20/12/16	James Hocking	Further update for RTTOV v12 release

## Contents

<b>1. Introduction .....</b>	<b>2</b>
<b>2. Implementation of DOM .....</b>	<b>3</b>
<b>3. Cloud overlap assumptions.....</b>	<b>4</b>
<b>4. Optical properties of scattering particles .....</b>	<b>5</b>
<b>5. Errors resulting from polychromatic calculations .....</b>	<b>5</b>
<b>6. Results of high spectral resolution vs RTTOV_DOM comparisons.....</b>	<b>8</b>
<b>7. Performance .....</b>	<b>12</b>
<b>8. Conclusions and future work .....</b>	<b>13</b>
<b>Acknowledgements.....</b>	<b>15</b>
<b>References.....</b>	<b>16</b>
<b>Appendix A – Discrete Ordinates Method overview .....</b>	<b>18</b>
<b>Appendix B – Input profiles used for validation of RTTOV_DOM .....</b>	<b>21</b>

## 1. Introduction

RTTOV is a fast radiative transfer model for simulating passive nadir-viewing visible, infra-red (IR) and microwave sensors (Saunders *et al* 1999). RTTOV supports IR sensors with channels in the range 0.4–50 $\mu$ m. RTTOV v11 (Hocking *et al* 2015) includes a parameterisation for scattering by aerosols, water clouds and ice clouds in the IR known as Chou-scaling (Chou *et al* 1999; Matricardi 2005) in which the scattering optical depth is scaled by the fraction of back-scattered radiation and the radiative transfer equation (RTE) is solved for emission/extinction only with no explicit treatment of scattering. This is very fast and has reasonable accuracy in treating the thermal emission source term in the presence of scattering particles: for example Martinet *et al* (2013) and Okamoto *et al* (2013) have demonstrated promising results in studies of assimilation of cloudy IR radiances in numerical weather prediction (NWP) systems using the RTTOV Chou-scaling approximation.

For solar-affected channels RTTOV v11 provides a calculation of the single-scattering contribution due to aerosols and clouds from the solar source term, but in general the resulting radiances exhibit very large errors as multiple scattering cannot be neglected at visible and near-IR wavelengths. At wavelengths below 2 $\mu$ m there is also a single-scattering calculation to account for molecular Rayleigh scattering which is described in Saunders *et al* (2013).

This report describes the implementation of the Discrete Ordinates Method (DOM) pseudo-exact multiple-scattering algorithm (Chandrasekhar 1960) for clouds and aerosols in RTTOV. The new model is referred to as RTTOV\_DOM and this has been implemented in RTTOV v12, the next major version due to be released in December 2016.

Sections 2-4 describe the implementation of scattering in RTTOV\_DOM and the calculation of the optical properties of the scattering particles. Section 5 describes the simulations carried out to understand some of the errors in the RTTOV\_DOM simulations and section 6 presents the results of these simulations. Section 7 considers the computational performance of RTTOV\_DOM and section 8 concludes the report with a look to future work.

## 2. Implementation of DOM

DOM as implemented in RTTOV\_DOM follows the implementation of DOM in DISORT (Stamnes *et al* 1988) reasonably closely. DISORT is a well-established solver for the one-dimensional radiative transfer equation (RTE). Since DISORT and more generally DOM are very well documented the details of the method are not repeated here. A brief description of the algorithm is given in Appendix A. The differences between DISORT and RTTOV\_DOM are discussed below.

Both the solar and thermal source terms are implemented in RTTOV\_DOM: it is possible to choose between Chou-scaling and DOM for treating the thermal source term. RTTOV ignores the solar source term for channels above  $5\mu\text{m}$  and ignores the thermal source term for channels below  $3\mu\text{m}$ . RTTOV\_DOM allows the number of streams (discrete ordinates) to be selected from two upwards. The accuracy parameter in DISORT which is used to exit the azimuthal loop once the radiance increments become sufficiently small is also present in RTTOV\_DOM. Currently RTTOV\_DOM treats the surface as a Lambertian reflector.

By default RTTOV accounts for variation in the local angle of the radiation path through the atmosphere due to the Earth's curvature and also optionally due to refraction. However RTTOV\_DOM requires a strictly plane-parallel geometry so an option has been added to RTTOV\_DOM to select this and the option is automatically enforced whenever DOM calculations are performed. One advantage of providing an option for this is that the plane geometry can be turned on for Chou-scaling simulations allowing more direct comparisons with the full multiple-scattering calculations. The option applies to both clear-sky and scattering simulations.

The main difference between RTTOV\_DOM and DISORT is that for solar simulations RTTOV\_DOM takes the full phase functions as input and directly interpolates them at the scattering angle where required whereas DISORT reconstructs the phase function from the full Legendre expansion. The latter is not a practical solution for some phase functions at visible wavelengths which may require many thousands of Legendre terms in order to be accurately reconstructed. RTTOV v12 therefore only requires as many Legendre coefficients as there are Discrete Ordinates (or “streams”) in the calculation.

In the current implementation RTTOV\_DOM assumes the surface is Lambertian. Future implementations may provide the option of alternative BRDF models.

To aid validation of the implementation a version of RTTOV has also been created which calls DISORT to carry out the integration of the RTE, henceforth referred to as RTTOV\_DISORT. The code is almost identical to RTTOV\_DOM with the exception that DISORT is called to solve the RTE. In order to provide strictly comparable outputs from RTTOV\_DOM and RTTOV\_DISORT, the DISORT source was modified to make the Planck emission source term identical to that used in RTTOV\_DOM and to use the interpolated phase function instead of reconstructing it from the full Legendre decomposition.

When equivalent inputs are provided, the output radiances from RTTOV\_DOM and RTTOV\_DISORT agree to at least the fourth significant figure in all cases tested. However RTTOV\_DOM benefits from having DOM implemented inside RTTOV enabling re-use of calculation results and other optimisations. As such RTTOV\_DOM varies from being around two times to upwards of 200 times faster than RTTOV\_DISORT for any given simulation. Note however that the comparison is not a reflection on DISORT, but may mitigate some misgivings that the RTTOV implementation of DOM is *extremely* slow.

### **3. Cloud overlap assumptions**

For infrared cloudy simulations RTTOV implements the maximum-random overlap algorithm (Matricardi 2005). This results in a series of cloudy columns each with a unique distribution of clouds among layers. The RTE is solved for each cloudy column and for the clear column and the resulting radiances are linearly combined with weights determined by the overlap algorithm. When activated, aerosol scattering calculations affect all cloud columns (when clouds are present) and also the “clear” column.

For complex cloudy profiles this scheme can result in a large number of cloudy columns and as such it can be expensive in both memory and run-time. It is possible to ignore cloud columns with very small weights using RTTOV’s “cldstr\_threshold” parameter which can speed up simulations in some circumstances. It is planned to identify a computationally cheaper alternative to this overlap scheme in the future.

As an aside, this is one example where the embedded nature of the DOM implementation inside RTTOV enables results from previous calculations (cloud columns) to be re-used to obtain a significant speed-up over RTTOV\_DISORT which has to treat each cloud column completely independently.

#### **4. Optical properties of scattering particles**

RTTOV provides optical properties calculated using Mie theory assuming spherical particles for a pre-defined selection of aerosols and water cloud particles (Matricardi 2005). For ice clouds a parameterisation of the Baran ice optical property database is available (Saunders *et al* 2013). Alternatively it is possible to input vertical profiles of the scattering optical properties for each channel explicitly. For DOM the required optical properties are the absorption and scattering coefficients, the Legendre coefficients of the phase function decomposition and, for solar simulations, the explicit phase function.

RTTOV\_DOM provides the same options for aerosol and cloud liquid water particle types and for the explicit input of optical properties. The parameterisation of the Baran database has been extended to the visible/near-IR for RTTOV v12. In addition the SSEC ice optical property database (Baum *et al* 2011) may be used which expresses optical properties in terms of wavelength and effective particle diameter (Deff). The Deff in RTTOV may be supplied explicitly or can be calculated using one of four parameterisations: in this paper the McFarquhar (2003) parameterisation is used which expresses Deff in terms of ice water content. The Baran database has no explicit dependence on particle size.

Legendre decompositions of the phase functions are calculated by first interpolating the phase functions onto a 1000-point (liquid water particles) or 8000-point (ice particles) Gaussian quadrature using spline interpolation. The quadrature is then used to derive the Legendre coefficients. The coefficient files for RTTOV\_DOM contain up to 128 Legendre coefficients (there can be fewer if the coefficients drop below  $10^{-6}$  in magnitude). The number of Legendre coefficients required in the simulations is equal to the user-selected number of DOM streams. Therefore the maximum number of DOM streams is 128 when using the supplied optical properties. If users supply their own optical properties there is no fixed upper limit to the number of streams.

#### **5. Errors resulting from polychromatic calculations**

The core of the RTTOV model is the fast and accurate prediction of layer optical depths due to gaseous absorption for satellite sensor channels of finite spectral width. Therefore for any multiple-scattering scheme implemented in RTTOV only the predicted “polychromatic” optical depth profile calculated for the specified sun/satellite geometry is

available. DOM is a solver for the monochromatic RTE and as such the use of the polychromatic RTTOV optical depths will result in errors in simulated radiances.

In addition to the gaseous optical depths, the top of atmosphere (TOA) solar irradiance and the cloud or aerosol scattering properties also vary across the sensor channels: these variations are not accounted for in RTTOV\_DOM. The scattering properties are calculated at the channel central wavenumber and the TOA solar irradiance is obtained by integrating the solar spectrum over the channel spectral response function (SRF).

In order to attempt to characterise the errors which result from the RTTOV\_DOM polychromatic calculations, comparisons have been made of radiances from RTTOV\_DOM with pseudo-monochromatic radiances calculated from RTTOV\_DOM run at high spectral resolution across the instrument channel spectral range and integrated over each channel SRF. The comparison was carried out for the subset of channels from the MSG-3 SEVIRI sensor listed in Table 1.

<b>SEVIRI channel</b>	1	2	3	4	6	9	11
<b>Wavelength (<math>\mu\text{m}</math>)</b>	0.6	0.8	1.6	3.9	7.3	10.8	13.4

*Table 1: SEVIRI channels simulated in the HSR vs RTTOV comparisons*

Two atmospheric profiles were selected: the tropical and mid-latitude winter profiles from the AFGL atmospheric profile set (Anderson *et al* 1986). For each profile a single cloud spanning 2 or 3 layers was added consisting of either water cloud (based on the continental stratocumulus STCO particle type, Matricardi 2005) or ice cloud (derived from the SSEC database using the McFarquhar ice effective diameter parameterisation). In both cases the cloud fraction was set to one. The profile data are given in Appendix B.

In all simulations 16 DOM streams were used. The DOM accuracy parameter was set to zero and the RTTOV “cldstr\_threshold” parameter was set to  $10^{-8}$  (this has no impact on the simulated radiances, but can reduce run-time). Simulations were repeated for a variety of satellite and solar geometries. The simulations were also carried out for the clear-sky case: these used the standard RTTOV clear-sky code path which does *not* use DOM to solve the RTE. The configurations of the simulations are described below and the results are shown in the next section.



### **High spectral resolution simulations**

The high spectral resolution (HSR) simulations were carried out using gaseous optical depths calculated by LBLRTM v12.2 with the same fixed gas profiles as for the RTTOV coefficient training. LBLRTM was run at high spectral resolution ( $0.0001\text{ cm}^{-1}$ ) and the resulting layer optical depths were averaged at  $0.01\text{ cm}^{-1}$  in the thermal IR and  $0.1\text{ cm}^{-1}$  in the visible/near-IR and shortwave IR for the test profiles. The HSR simulations consist of the radiances from RTTOV\_DOM calculations carried out at these latter resolutions integrated over the channel SRFs.

The cloud optical properties were calculated at spectral intervals of  $10\text{ cm}^{-1}$  in the IR and  $100\text{ cm}^{-1}$  in the visible/near-IR across each channel. Since the optical properties vary relatively slowly with wavenumber (compared to the gaseous absorption) the HSR simulations used the optical properties for the nearest wavenumber in the pre-computed look-up table (i.e. no interpolation was performed).

The top-of-atmosphere solar irradiance was calculated from the Planck function evaluated assuming solar surface temperature 5900K, emissivity 0.99, solar radius  $6.96 \times 10^8\text{ km}$  and Earth-sun distance  $1.5 \times 10^{11}\text{ km}$ . Fidelity to the true values is not vital so long as consistent values are used in all simulations and the values exhibit realistic variation across the channel spectral intervals.

When RTTOV\_DOM was called, the “channel central wavenumber” was updated for each simulation across the channel spectral response. This affects the Rayleigh single-scattering in the visible channels and the thermal emission source term in the IR channels. The band correction coefficients (used by RTTOV to ensure the application of the Planck function at a single wavenumber is representative of the whole sensor channel) were reset to unit scale factor and zero offset for the HSR simulations.

### **RTTOV\_DOM simulations**

The standard RTTOV\_DOM simulations were carried out using the RTTOV v11.3 official “v9 predictor” MSG-3 SEVIRI RTTOV coefficient file on 54 levels. The cloud optical properties were calculated for the nominal channel central wavenumbers and the top of atmosphere solar irradiance was calculated using the parameters given above integrated over each channel SRF.

## 6. Results of high spectral resolution vs RTTOV\_DOM comparisons

### Visible, near-IR and short-wave IR channels

Figures 1-4 show the difference between the full HSR simulations and RTTOV\_DOM simulations for the clear-sky tropical profile for SEVIRI channels 1-4. Differences for channels 1-3 are expressed as % relative difference in radiance while the differences for channel 4 (and other IR channels) are expressed as brightness temperature (BT) differences.

One contribution to the increase in errors with larger satellite and solar zenith angles is the Rayleigh scattering: in the HSR simulations the variation in the Rayleigh contribution across the channel can be substantial in the channels at shorter wavelengths. Figures 5 and 6 compare the HSR radiances with those from RTTOV\_DOM where the channel central wavenumber (used to calculate the Rayleigh single-scattering) has been calculated from the average value of  $1/\lambda^4$  (where  $\lambda$  is wavelength) over the channel weighted by the spectral response. This acts to increase the contribution due to Rayleigh scattering because the wavelength calculated in this way is always smaller than the nominal channel central wavelength. In this case the negative biases are reduced, but positive biases are introduced in channel 1 at the highest zenith angles. Improvements to the treatment of Rayleigh scattering are planned for future versions of RTTOV. As clear-sky simulations are not the focus of this paper this is not discussed further here.

Figures 7-10 show the differences between the HSR and RTTOV\_DOM simulations for the tropical cloud liquid water profile. As noted above the cloud optical properties for RTTOV\_DOM are calculated at the channel nominal central wavenumber which takes no account of the variation in the properties across the channel. For the visible/near-IR channels the absorption and scattering coefficients are relatively constant across the channels, but the phase functions can vary substantially. For channel 4 there is greater variability in the absorption and scattering coefficients although the channel-averaged values do not differ very greatly from those calculated at the nominal central wavenumber, and again the phase function varies substantially across the channel. Figures 11-14 compare the HSR radiances with those from RTTOV\_DOM where the cloud optical properties for the latter are averaged across the channel spectral response. To calculate the averaged values the cloud properties used in the HSR simulations were linearly interpolated onto the wavenumbers over which the filter response was defined. In channels 1-3 the reduction in the differences is substantial. For channel 4 the differences change sign, but the magnitudes are similar.

Examination of the phase functions yields an explanation for these results: Figure 15 shows the relative differences between the channel-averaged phase functions and the phase functions calculated at the nominal central wavenumber for the visible/near-IR channels. The noise results from the discretisation of the size distribution when the optical properties are calculated. For IR channels a coarser resolution may be used without introducing this noise. The number of size bins was substantially increased from the value used for RTTOV v11 optical property calculations in order to reduce the size of these oscillations in visible channel phase functions to the magnitudes shown. The averaging of the phase functions across the channel smooths the noise. For channel 1 the difference at  $180^\circ$  is relatively large ( $\sim 4.5\%$ ) and it is this which causes the noticeable differences in the radiances for the zero relative azimuth case where the sun and satellite angles are equal (i.e. direct back-scatter) in Figure 7. These artefacts are not seen in Figure 11 where the channel-averaged phase functions are used.

In the case of channel 4 there are some systematic differences between the phase function at the central wavenumber and the channel-averaged phase function (Figure 16): the channel-averaged phase function is larger in the forward scattering direction (less than  $\sim 20^\circ$ ) and is smaller at larger scattering angles. It is not obvious why the channel-averaged phase function does not give smaller differences between the HSR and RTTOV\_DOM radiances in this case.

The results suggest that it may be worth calculating scattering optical properties by averaging them across the channel spectral response, at least for visible/near-IR channels and for cloud water particle types.

Figures 17-21 show the differences between the HSR and RTTOV\_DOM simulations for the tropical cloud ice water profile and figures 21-24 show the comparisons when the ice optical properties for the RTTOV\_DOM simulations are averaged over the channel SRF. For ice cloud the averaging of the optical properties across the channel SRF has neutral to negative impact on the differences. Examination of the phase functions (not shown) reveals that those calculated for the channel nominal central wavenumber are more similar to the channel-averaged phase functions than for the water cloud particle type for the visible/near-IR channels.

Figures 25-28 show the differences between the HSR and RTTOV\_DOM simulations for the tropical cloud liquid water profiles where the cloud optical properties do *not* vary across the channel for the HSR simulations: instead the default RTTOV\_DOM values

are used. These plots show only very small differences indicating that the variation in scattering properties across the channel accounts for a large proportion of the polychromatic errors. The equivalent plots for the cloud ice water profile are similar and are not shown.

Figures 29-48 show corresponding results for the mid-latitude winter case. Figures 29-32 show the clear-sky differences. Figures 33-36 show the differences for the cloud liquid water profile and Figures 37-40 show the differences when the RTTOV\_DOM simulations are run with channel-averaged optical properties. Figures 41-44 show the differences for the cloud ice profile and Figures 45-48 show the differences with the channel-averaged ice optical properties. The results for the mid-latitude profiles are generally consistent with those for the tropical case: there is some benefit in the channel averaged optical properties for the cloud liquid water particle type in the visible/near-IR channels (at least for channels 1 and 2), but not in channel 4, and there is no clear benefit to the channel-averaged properties for the ice cloud.

Overall these comparisons show good agreement can be obtained between the HSR and RTTOV\_DOM simulations, especially for the visible/near-IR channels, for which the radiances differ by less than 1% in many cases. The results suggest that perhaps water cloud optical properties should be averaged over channel SRFs for visible/near-IR channels although this adds complexity to the optical property calculation which should be justified by further investigation. The comparisons give confidence that the polychromatic nature of the RTTOV\_DOM simulations is not causing fundamental problems. The largest contribution to the polychromatic errors in these solar-affected channels is from the variation in cloud optical properties across the channels.

### **IR channels**

Figures 49-51 show the BT differences in the IR SEVIRI channels for the HSR and RTTOV\_DOM simulations for the tropical profile. Figures 52-54 show the same for the mid-latitude winter profile. Figures 55-58 show the cloud liquid and ice water results with channel-averaged cloud optical properties.

The impact of the polychromatic gas absorption is relatively large for the water vapour and CO<sub>2</sub> channels (channels 6 and 11 respectively). This is particularly true in channel 11 for which there is a large variation in atmospheric transmittance across the channel: such variability is more difficult to parameterise accurately in the RTTOV optical depth regression and this is reflected in the larger observed differences for this channel. The

differences observed for the clear-sky profiles here are consistent with the statistics produced by the RTTOV coefficient generation comparing RTTOV brightness temperatures with those from high spectral resolution simulations. The “v7 predictor” RTTOV coefficients exhibit much smaller errors in SEVIRI channel 11 than the “v9 predictor” coefficients used in this study. This may be due to the fact that the v9 predictors were originally created for simulating radiances for hyperspectral instruments and as such are sub-optimal for sensors with relatively broad channels.

The cloud liquid and ice water absorption and scattering coefficients in these two channels vary almost linearly across the channel responses and the channel-averaged phase functions are quite similar to the phase functions at the channel central wavenumbers (see for example Figure 16). Therefore the largest contribution to the differences in these two channels comes from the gaseous absorption: there are errors due to the RTTOV gaseous optical depth regression and also errors due to these polychromatic optical depths being used in the DOM algorithm for the cloudy profiles. The channel-averaged optical properties have almost no effect on the differences in these two channels. The differences between the HSR and RTTOV\_DOM simulations decrease in the presence of cloud because the absorption due to the cloud reduces the impact of the errors due to the polychromatic gas optical depths. The ice cloud is more highly absorbing than the water cloud and as a result exhibits the smallest differences.

The IR window channel 9 at  $10.8\mu\text{m}$  has much less gaseous absorption so the gas optical depths contribute less to the observed differences. There is substantial variation in the cloud liquid and ice absorption coefficients and (more especially) in the scattering coefficients across the channel for cloud liquid water. For cloud ice water, the channel-averaged phase function exhibits large relative differences (tens of %) compared to the nominal phase function, although the treatment of the thermal emission source term is less sensitive to differences in the phase function than treatment of the solar source term. In this case the channel-averaged cloud properties do reduce the differences for both the liquid and ice water clouds, but the differences are rather small in the non-averaged case anyway so there is only a small absolute benefit.

As in the case of the solar-affected channels, the results do not show any fundamental problems with applying the DOM algorithm to the polychromatic RTTOV simulations in the thermal IR. The implementation of DOM is intended primarily for the treatment of solar scattering since the Chou-scaling offers a very fast and reasonably accurate treatment of the thermal emission term as already described. However DOM may be

useful for validating the Chou-scaling or obtaining more accurate scattering results in the thermal IR at a cost in execution time.

## **7. Performance**

In RTTOV the RTE is integrated on the layers defined by the pressure levels input by the user. The cost of the DOM solver is strongly dependent on the number of layers for which the RTE is being solved. Therefore any technique or modification which can reduce the number of layers will speed up the code significantly. This is one of the reasons why molecular Rayleigh multiple-scattering is not treated in RTTOV\_DOM: (almost) every layer would contain scattering material and even though phase function is relatively simple the computations would still be very expensive.

The DOM solution for clear layers (those containing no scattering particles) is trivial in the visible and near-IR as there is no source term. In the shortwave RTTOV\_DOM combines adjacent clear layers together into a single layer: this can result in significant performance gains with no impact on simulated radiances. This is not possible for thermal IR channels since the thermal source term is temperature-dependent so one will compromise the accuracy of the solution unless the layers happen to share the same temperature.

For thermal IR channels where absorption by gas, cloud and/or aerosol can be significant it is possible that at some level the atmosphere becomes opaque such that layers below this are not visible to the sensor. These lower layers can optionally be ignored by RTTOV\_DOM. This has no effect on simulated radiances if the threshold defining “opaque” is sufficiently large: this parameter is user-configurable.

One potential further improvement might be to allow users to specify the cloud/aerosol profiles on a different (reduced) set of layers or to enable some way to flag that consecutive scattering layers contain particles with identical scattering parameters and particle densities: where there is no thermal source term (in the visible/near-IR) these layers could be combined together with no impact on radiances, but with substantial savings in computation. Again this is more difficult in the IR due to the dependence on layer temperature of the emission source term.

It is worth noting that performance of RTTOV\_DOM in the IR is not a major concern as most users are expected to prefer the more efficient Chou-scaling approach.

If users are concerned about speed then they should consider setting cloud/aerosol amounts to zero in layers where otherwise the values would be very small. For direct-model-only cloudy simulations eliminating cloud columns with very small weights using the RTTOV “cldstr\_threshold” parameter is recommended. However there are fundamental limits to what can be achieved in respect of optimising the DOM algorithm. In the future it is planned to incorporate the MFASIS fast visible scattering parameterisation (Scheck 2015) into RTTOV alongside the DOM implementation.

## **8. Conclusions and future work**

The Discrete Ordinates Method has been successfully implemented in RTTOV v12 and produces essentially identical radiances to a similar version of RTTOV which calls the DISORT model. The new RTTOV\_DOM model has been compared to pseudo-monochromatic radiances calculated at high spectral resolution across the spectral intervals of a selection of MSG-3 SEVIRI channels and integrated over the channel SRFs. The comparisons indicate that it is the variation in cloud scattering properties across each channel which contributes most to the observed differences in the visible/near-IR channels while in the IR the variable gas absorption across the channels dominates the differences between the RTTOV\_DOM and HSR simulations.

The results suggest that for visible/near-IR channels there may be some benefit in averaging the optical properties across the channel SRFs, at least for water cloud particle types. This can be investigated further, for example by comparisons against observations, to see if the increased complexity is worthwhile in practical applications. This only affects the optical properties provided to RTTOV via the input coefficient files and these can be updated independently of the code.

The simulations indicate that in the visible/near-IR the errors due to the polychromatic nature of the RTTOV\_DOM simulations are of the order of 1-2%. In the 3.9 $\mu$ m channel (channel 4) the errors can reach 1-2K: this is perhaps not surprising as this channel is spectrally comparatively broad and there can be significant variability in the phase function across the channel. For IR channels with significant gas absorption the errors are dominated by the gaseous absorption and the presence of cloud mitigates the

errors. For the IR window channel the polychromatic errors are small especially for satellite zenith angles below 60°. The results do not suggest that any particularly large errors result specifically from the application of DOM to the simulation of sensor channels with finite spectral width.

In addition to the direct model implementation of DOM, RTTOV v12 includes the tangent linear (TL), adjoint (AD) and Jacobian (K) models. These are relatively expensive in run-time and in memory requirements, but may be of use in research applications. Some possible further developments are described below: these options for future work will be considered for future releases of RTTOV.

### **Molecular Rayleigh scattering**

Currently the extinction due to Rayleigh scattering is accounted for in the LBLRTM simulations used to train RTTOV. This provides a good approximation to the true extinction as the effect is integrated over the channel spectral response. The single-scattering contribution of Rayleigh scattering is calculated within RTTOV for the channel nominal central wavelength. This will always under-estimate the true contribution of Rayleigh scattering. It may be worth investigating whether a more optimal wavelength can be chosen to better represent each channel.

To treat Rayleigh multiple-scattering using DOM is too expensive. However it may be worth investigating the possibility of parameterising the Rayleigh multiple-scattering, at least for clear-sky simulations. This would involve the Rayleigh scattering extinction being calculated (parameterised) within RTTOV and therefore it would have to be excluded from the LBLRTM simulations (requiring the LBL database to be recreated and all visible/near-IR coefficient files to be regenerated). There is not a simple way to fully treat Rayleigh multiple-scattering alongside multiple-scattering by clouds and aerosols without a substantial cost in computational resources. While the Rayleigh extinction is included in the LBLRTM simulations it is not even possible for users to treat the Rayleigh scattering using RTTOV\_DOM themselves (in theory users could do this by specifying the Rayleigh scattering parameters explicitly as if it were an aerosol).

Note that Scheck (2016) demonstrates that RTTOV\_DOM can introduce significant errors in simulated radiances by ignoring the multiple-scattering interaction between Rayleigh scattering and clouds/aerosols, particularly as the cloud (or aerosol) optical thickness increases. It is planned to integrate the MFASIS fast model (Scheck 2015) into RTTOV which can account for these effects.



### **Scientific enhancements**

Currently RTTOV\_DOM treats the surface as a Lambertian reflector. It would be difficult to incorporate arbitrary BRDFs into RTTOV, but it would be possible to implement a small selection of common analytical BRDFs among which the user could choose.

Although the strict plane-parallel assumption is required for the surface-to-sensor path (otherwise the calculations become messy and inevitably more costly), it is possible to take account of the spherical geometry and atmospheric refraction (as classical RTTOV does) for the sun-to-surface path in the treatment of the direct solar beam which can improve accuracy for simulations with larger solar zenith angles. This is done, for example, in the LIDORT model (Spurr *et al* 2001, Spurr 2002).

### **Performance enhancements**

The primary way to decrease run-time in DOM simulations is to reduce the number of layers for which the RTE is being solved. It could be worth introducing some method to allow users to group input layers together which share scattering properties: for visible/near-IR channels such layers could be treated together in the DOM algorithm with substantial performance benefits.

For some applications a two-stream solution may be sufficiently accurate and it may be possible to write an optimised special case for this.

In addition to reducing the run-time it would also be beneficial to minimise the memory footprint of the DOM solver. Steps have already been taken to avoid wasteful memory allocations, but it may be possible to go further. In addition it is planned to identify alternative approaches to the treatment of cloud overlap which are less memory intensive and such schemes will also enable faster simulations in the future.

Finally it is likely that other implementations of DOM such as LIDORT have introduced optimisations which could be applied to RTTOV\_DOM: this will also be investigated.

### **Acknowledgements**

RTTOV is developed within the EUMETSAT Satellite Applications Facility for Numerical Weather Prediction (NWP SAF) with contributions from the Met Office, Météo-France and ECMWF.

## References

Anderson, G.P., J.H. Chetwynd. S.A. Clough. E.P. Shettle. F.X. Kneizys, 1986: AFGL Atmospheric Constituent Profiles (0-120km). *Air Force Geophysics Laboratory report AFGL-TR-86-0110*.

Baum, B. A., P. Yang, A. J. Heymsfield, C. Schmitt, Y. Xie, A. Bansemer, Y. X. Hu, and Z. Zhang, 2011: Improvements to shortwave bulk scattering and absorption models for the remote sensing of ice clouds. *J. Appl. Meteor. Clim.*, 50, 1037-1056.

Chandrasekhar, S. 1960: *Radiative Transfer* (Dover, New York).

Chou, M.-D., K.-T. Lee, S.-C. Tsay, and Q. Fu, 1999: Parameterization for cloud longwave scattering for use in atmospheric models. *J. Clim.*, 12, pp. 159-169.

Hocking, J., P.J. Rayer, D. Rundle, R.W. Saunders, M. Matricardi, A. Geer, P. Brunel and J. Vidot, 2014: RTTOV v11 Users Guide  
[http://nwpsaf.eu/deliverables/rm/docs\\_rttov11/users\\_guide\\_11\\_v1.4.pdf](http://nwpsaf.eu/deliverables/rm/docs_rttov11/users_guide_11_v1.4.pdf)

Martinet, P., N. Fourrié, V. Guidard, F. Rabier, T. Montmerle and P. Brunel, 2013: Towards the use of microphysical variables for the assimilation of cloud-affected infrared radiances. . *Q. J. R. Meteorol. Soc.*, 139, 1402-1416.

Matricardi, M., 2005: The inclusion of aerosols and clouds in RTIASI, the ECMWF fast radiative transfer model for the Infrared Atmospheric Sounding Interferometer. *ECMWF Technical Memorandum 474*.

McFarquhar, G.M., S. Iacobellis and R.C.J. Somerville, 2003: SCM simulations of tropical ice clouds using observationally based parameterizations of microphysics. *J. Clim.*, 16, 1643-1664.

Okamoto K., A.P. McNally, and W. Bell, 2013: Progress towards the assimilation of all-sky infrared radiances: an evaluation of cloud effects *Q. J. R. Meteorol. Soc.*, 140, 1603-1614  
Saunders R.W., M. Matricardi and P. Brunel, 1999: An improved fast radiative transfer model for assimilation of satellite radiance observations. *Q. J. R. Meteorol. Soc.*, 125, 1407-1425.

Saunders R.W., J. Hocking, D. Rundle, P.J. Rayer, M. Matricardi, A. Geer, C. Lupu, P. Brunel and J. Vidot, 2013: RTTOV v11 Science and Validation Report  
[http://nwpsaf.eu/deliverables/rm/docs\\_rttov11/rttov11\\_svr.pdf](http://nwpsaf.eu/deliverables/rm/docs_rttov11/rttov11_svr.pdf)

Scheck L., 2015: MFASIS - a fast radiative transfer method for the visible spectrum. *NWP SAF report* [http://nwpsaf.eu/vs\\_reports/nwpsaf-mo-vs-051.pdf](http://nwpsaf.eu/vs_reports/nwpsaf-mo-vs-051.pdf)

Scheck, L., 2016: Comparison of MFASIS and RTTOV-DOM. *NWP SAF report* [http://nwpsaf.eu/vs\\_reports/nwpsaf-mo-vs-054.pdf](http://nwpsaf.eu/vs_reports/nwpsaf-mo-vs-054.pdf)

Spurr, R., T. Kurosu, and K. Chance, 2001: A linearized discrete ordinate radiative transfer model for atmospheric remote sensing retrieval. *J. Quant. Spectrosc. Radiat. Transfer*, 68, 689–735, 2001.

Spurr, R.J.D., 2002: Simultaneous radiative transfer derivation of intensities and weighting functions in a general pseudo-spherical treatment, *J. Quant. Spectrosc. Radiat. Transfer*, 75, 129-175.

Stamnes, K., S.-C. Tsay, W. Wiscombe and K. Jayaweera, 1988: Numerically stable algorithm for discrete-ordinate-method radiative transfer in multiple-scattering and emitting layered media. *Applied Optics*, 27, 2502-2509.

Zdunkowski, W., T. Trautmann and A. Bott, 2007: *Radiation in the Atmosphere* (Cambridge University Press, Cambridge).

## Appendix A – Discrete Ordinates Method overview

A brief overview of the Discrete Ordinates Method is given here: the full mathematical formulation can be found in numerous sources such as Stamnes *et al* (1988) or Zdunkowski *et al* (2007).

The radiance field for a plane-parallel atmosphere is expressed as a function of optical depth to space  $\tau$ , the secant of the zenith angle  $\mu$ , and the azimuth angle  $\varphi$ . The azimuthal dependence is separated by expressing the radiance as a discrete cosine series:

$$I(\tau, \mu, \varphi) = \sum_{m=0}^{\infty} (2 - \delta_{0m}) I^m(\tau, \mu) \cos m(\varphi - \varphi_0)$$

where  $\delta_{ij}$  is the Kronecker delta ( $\delta_{ij} = 1$  if  $i = j$  and  $\delta_{ij} = 0$  otherwise). Similarly, the phase functions  $P$  defined over scattering angle  $\Theta$  (for incoming direction  $\mu, \varphi$  and outgoing direction  $\mu', \varphi'$ ) are decomposed into a series of Legendre polynomials:

$$\begin{aligned} P(\cos \Theta) &= P(\mu, \varphi, \mu', \varphi') \\ &= \sum_{m=0}^{\infty} (2 - \delta_{0m}) \sum_{l=m}^{\infty} p_l^m P_l^m(\mu) P_l^m(\mu') \cos m(\varphi - \varphi') \end{aligned}$$

where  $P_l^m$  are the associated Legendre polynomials and  $p_l^m$  are the Legendre coefficients.

The radiative transfer equation (RTE) for each azimuthal component can be written:

$$\begin{aligned} \mu \frac{d}{d\tau} I^m(\tau, \mu) &= I^m(\tau, \mu) - \frac{\omega_0}{2} \int_{-1}^1 \sum_{l=m}^{\infty} p_l^m P_l^m(\mu) P_l^m(\mu') I^m(\tau, \mu') d\mu' \\ &\quad - \frac{\omega_0}{4\pi} S_0 \exp\left(-\frac{\tau}{\mu_0}\right) \sum_{l=m}^{\infty} p_l^m P_l^m(\mu) P_l^m(\mu_0) - (1 - \omega_0) B(\tau) \delta_{0m} \end{aligned}$$

where  $\omega_0$  is the single-scattering albedo,  $S_0$  is the TOA solar irradiance,  $\mu_0$  is the secant of the solar zenith angle and  $B(\tau)$  is the Planck function evaluated at the temperature at level  $\tau$ .

To compute the integral in this equation Gaussian quadrature is used. For a function  $f$  one can define an  $N$ -point quadrature with points  $q_i$  and associated weights  $w_i$  ( $i=1, \dots, N$ ) such that:

$$\int_{-1}^1 f(x) dx \approx \sum_{i=1}^N w_i f(q_i)$$

DOM uses a quadrature of size  $N$  over the cosine of the zenith angle to account for radiances travelling in a discrete set of directions. The more directions (quadrature points or “streams”) used the more accurate the simulation and the slower it runs.

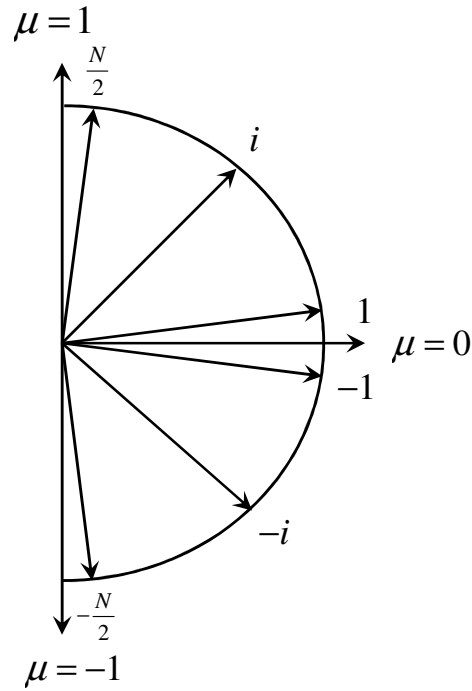


Figure A.1: discretisation of  $I(\tau, \mu)$  into  $N$  streams.  
Illustration taken from Zdunkowski et al (2007)

The RTE for an homogenous layer for each stream  $i=1, \dots, N$  can then be written:

$$\begin{aligned} \mu_i \frac{d}{d\tau} I^m(\tau, \mu_i) &= I^m(\tau, \mu_i) - \frac{\omega_0}{2} \sum_{j=1}^N w_j I^m(\tau, \mu_j) \sum_{l=m}^N p_l^m P_l^m(\mu_i) P_l^m(\mu_j) \\ &\quad - \frac{\omega_0}{4\pi} S_0 \exp\left(-\frac{\tau}{\mu_0}\right) \sum_{l=m}^N p_l^m P_l^m(\mu_i) P_l^m(\mu_0) \end{aligned}$$

This defines a system of  $N$  ordinary differential equations representing the radiance travelling in each quadrature direction which can be solved for each atmospheric layer to obtain expressions for these radiances.

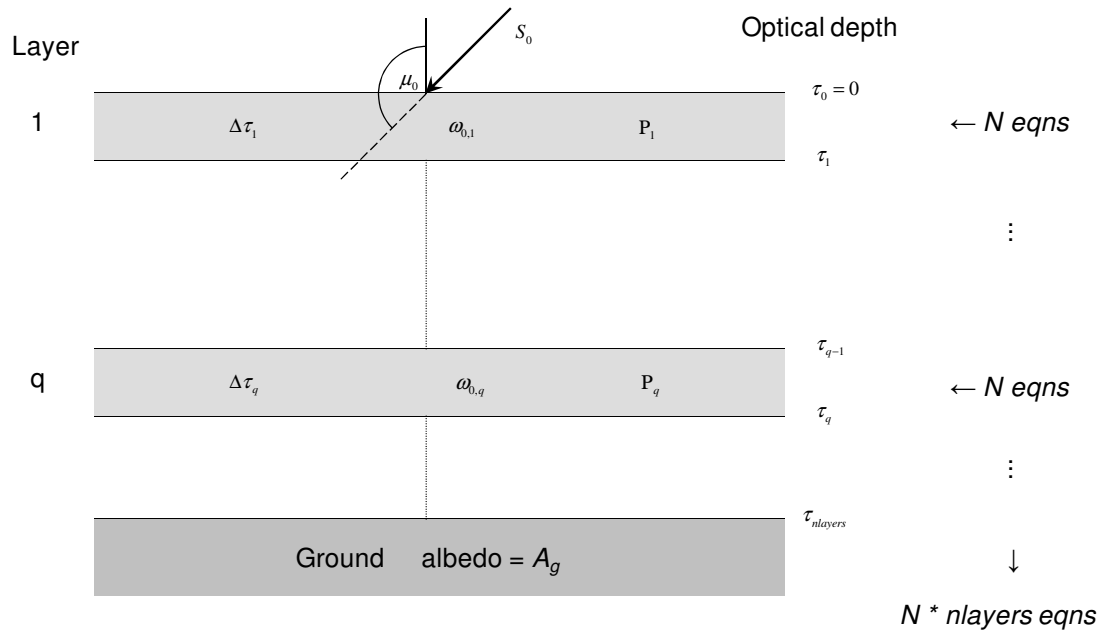


Figure A.2: subdivision of atmosphere into  $n$  layers homogenous layers with optical depths  $\Delta\tau_q$ , single scattering albedos  $\omega_{0,q}$  and phase functions  $P_q$  for  $q=1, \dots, n$  layers. Illustration taken from Zdankowski et al (2007)

The solutions for the individual layers are combined into a system of  $N * nlayers$  linear equations determined by the boundary conditions:

- zero downwelling diffuse radiances at the top of atmosphere
- radiances for each stream must be continuous at each layer interface
- upwelling and downwelling radiances at the surface are related to one another according to the surface albedo.

This linear system is solved and it is then possible to write down an expression for the radiance in any direction at any point in the atmosphere (details omitted here, see for example Stamnes et al 1988).

## Appendix B – Input profiles used for validation of RTTOV\_DOM

Tables B.1 and B.2 show the input profiles of pressure, temperature, water vapour and ozone and the cloud liquid and ice water and cloud fraction profiles for the AFGL tropical and mid-latitude winter atmospheres. Note that the cloud properties are defined for the layers bounded by the pressure levels. The test simulations included either no cloud (clear-sky), cloud liquid water (CLW) only or cloud ice water (CIW) only.

The surface properties that were used for the two profiles are given below:

	Tropical	Mid-lat winter
<b>T skin</b>	302.0 K	272.2 K
<b>p 2m</b>	1040.0 hPa	1040.0 hPa
<b>T 2m</b>	300.0 K	272.2 K
<b>q 2m</b>	25000 ppmv	4400 ppmv
<b>latitude</b>	15°	45°

A surface emissivity of 0.98 was used for thermal IR channels and a surface BRDF of 0.1 was used for visible/near-IR channels. For the 3.9 $\mu$ m channel the emissivity and BRDF were set to 0.98 and 0.0064 respectively which are consistent with one another for a Lambertian surface.

**Table B.1: Tropical atmosphere**

p (hPa)	T (K)	q (ppmv)	o3 (ppmv)	CLW (g/kg)	CIW (g/kg)	cfrac
5.00E-003	1.78E+002	1.41E+000	4.76E-001	0	0	0
1.31E-002	1.88E+002	2.34E+000	3.00E-001	0	0	0
3.04E-002	2.05E+002	3.53E+000	2.03E-001	0	0	0
6.44E-002	2.21E+002	4.63E+000	3.50E-001	0	0	0
1.26E-001	2.37E+002	5.44E+000	6.78E-001	0	0	0
2.32E-001	2.52E+002	5.98E+000	1.08E+000	0	0	0
4.05E-001	2.62E+002	6.00E+000	1.67E+000	0	0	0
6.75E-001	2.68E+002	6.00E+000	2.42E+000	0	0	0
1.08E+000	2.70E+002	5.92E+000	3.30E+000	0	0	0
1.67E+000	2.64E+002	5.67E+000	4.71E+000	0	0	0
2.50E+000	2.57E+002	5.38E+000	6.53E+000	0	0	0
3.65E+000	2.51E+002	5.04E+000	8.19E+000	0	0	0
5.19E+000	2.45E+002	4.73E+000	9.32E+000	0	0	0
7.22E+000	2.40E+002	4.44E+000	9.78E+000	0	0	0
9.84E+000	2.36E+002	4.18E+000	9.63E+000	0	0	0
1.32E+001	2.31E+002	3.92E+000	8.99E+000	0	0	0
1.73E+001	2.27E+002	3.62E+000	7.87E+000	0	0	0
2.25E+001	2.23E+002	3.38E+000	6.26E+000	0	0	0
2.87E+001	2.20E+002	3.21E+000	4.62E+000	0	0	0
3.62E+001	2.16E+002	2.88E+000	3.19E+000	0	0	0
4.50E+001	2.12E+002	2.71E+000	2.04E+000	0	0	0

5.54E+001	2.07E+002	2.61E+000	1.45E+000	0	0	0
6.75E+001	2.02E+002	2.61E+000	9.14E-001	0	0	0
8.14E+001	1.98E+002	2.78E+000	4.55E-001	0	0	0
9.72E+001	1.95E+002	2.92E+000	2.27E-001	0	0	0
1.15E+002	1.98E+002	3.20E+000	1.41E-001	0	0	0
1.35E+002	2.05E+002	4.28E+000	1.23E-001	0	0	0
1.57E+002	2.11E+002	6.35E+000	1.05E-001	0	0	0
1.81E+002	2.17E+002	9.79E+000	9.33E-002	0	0	0
2.08E+002	2.23E+002	2.59E+001	8.06E-002	0	0.5	1
2.36E+002	2.28E+002	5.99E+001	6.97E-002	0	0.5	1
2.67E+002	2.34E+002	1.36E+002	6.07E-002	0	0	0
3.00E+002	2.39E+002	2.66E+002	5.39E-002	0	0	0
3.35E+002	2.44E+002	4.55E+002	4.93E-002	0	0	0
3.72E+002	2.49E+002	7.19E+002	4.53E-002	0	0	0
4.10E+002	2.54E+002	1.08E+003	4.32E-002	0	0	0
4.50E+002	2.59E+002	1.54E+003	4.14E-002	0	0	0
4.91E+002	2.63E+002	2.08E+003	3.99E-002	0	0	0
5.33E+002	2.68E+002	2.87E+003	3.84E-002	0	0	0
5.75E+002	2.72E+002	3.58E+003	3.71E-002	0.5	0	1
6.18E+002	2.76E+002	4.21E+003	3.59E-002	0.5	0	1
6.61E+002	2.79E+002	5.88E+003	3.52E-002	0	0	0
7.04E+002	2.83E+002	7.99E+003	3.48E-002	0	0	0
7.45E+002	2.85E+002	1.09E+004	3.41E-002	0	0	0
7.86E+002	2.87E+002	1.38E+004	3.33E-002	0	0	0
8.26E+002	2.89E+002	1.60E+004	3.25E-002	0	0	0
8.63E+002	2.91E+002	1.75E+004	3.17E-002	0	0	0
8.99E+002	2.93E+002	1.89E+004	3.10E-002	0	0	0
9.32E+002	2.95E+002	2.08E+004	3.01E-002	0	0	0
9.62E+002	2.97E+002	2.25E+004	2.93E-002	0	0	0
9.89E+002	2.98E+002	2.40E+004	2.86E-002	0	0	0
1.01E+003	3.00E+002	2.53E+004	2.80E-002	0	0	0
1.03E+003	3.01E+002	2.64E+004	2.75E-002	0	0	0
1.05E+003	3.02E+002	2.72E+004	2.70E-002			

**Table B.2: Mid-latitude winter atmosphere**

p (hPa)	T (K)	q (ppmv)	o3 (ppmv)	CLW (g/kg)	CIW (g/kg)	cfrac
5.00E-003	2.01E+002	1.41E+000	5.14E-001	0	0	0
1.31E-002	2.13E+002	2.22E+000	2.36E-001	0	0	0
3.04E-002	2.25E+002	2.95E+000	2.79E-001	0	0	0
6.44E-002	2.35E+002	3.61E+000	4.23E-001	0	0	0
1.26E-001	2.45E+002	4.21E+000	7.38E-001	0	0	0
2.32E-001	2.54E+002	4.61E+000	1.23E+000	0	0	0
4.05E-001	2.62E+002	4.87E+000	1.89E+000	0	0	0
6.75E-001	2.66E+002	4.95E+000	2.73E+000	0	0	0
1.08E+000	2.62E+002	5.00E+000	4.10E+000	0	0	0
1.67E+000	2.53E+002	5.00E+000	5.61E+000	0	0	0
2.50E+000	2.43E+002	4.95E+000	6.87E+000	0	0	0
3.65E+000	2.35E+002	4.90E+000	7.20E+000	0	0	0
5.19E+000	2.28E+002	4.85E+000	7.10E+000	0	0	0
7.22E+000	2.21E+002	4.81E+000	6.84E+000	0	0	0



9.84E+000	2.18E+002	4.77E+000	6.32E+000	0	0	0
1.32E+001	2.17E+002	4.73E+000	5.88E+000	0	0	0
1.73E+001	2.15E+002	4.69E+000	5.53E+000	0	0	0
2.25E+001	2.15E+002	4.66E+000	5.21E+000	0	0	0
2.87E+001	2.15E+002	4.60E+000	4.69E+000	0	0	0
3.62E+001	2.15E+002	4.54E+000	4.10E+000	0	0	0
4.50E+001	2.15E+002	4.50E+000	3.54E+000	0	0	0
5.54E+001	2.15E+002	4.50E+000	2.78E+000	0	0	0
6.75E+001	2.15E+002	4.50E+000	2.07E+000	0	0	0
8.14E+001	2.16E+002	4.50E+000	1.54E+000	0	0	0
9.72E+001	2.17E+002	4.58E+000	1.17E+000	0	0	0
1.15E+002	2.17E+002	4.68E+000	9.31E-001	0	0	0
1.35E+002	2.18E+002	4.79E+000	8.14E-001	0	0	0
1.57E+002	2.18E+002	4.97E+000	7.20E-001	0	0	0
1.81E+002	2.19E+002	5.75E+000	5.68E-001	0	0.1	1
2.08E+002	2.19E+002	8.52E+000	4.22E-001	0	0.2	1
2.36E+002	2.19E+002	1.91E+001	3.04E-001	0	0.4	1
2.67E+002	2.21E+002	3.63E+001	2.16E-001	0	0	0
3.00E+002	2.26E+002	5.65E+001	1.56E-001	0	0	0
3.35E+002	2.30E+002	9.49E+001	1.17E-001	0	0	0
3.72E+002	2.34E+002	1.65E+002	9.23E-002	0	0	0
4.10E+002	2.39E+002	2.72E+002	7.59E-002	0	0	0
4.50E+002	2.42E+002	4.54E+002	6.25E-002	0	0	0
4.91E+002	2.46E+002	6.43E+002	5.36E-002	0	0	0
5.33E+002	2.50E+002	8.32E+002	4.70E-002	0	0	0
5.75E+002	2.53E+002	1.09E+003	4.04E-002	0	0	0
6.18E+002	2.56E+002	1.38E+003	3.52E-002	0	0	0
6.61E+002	2.59E+002	1.79E+003	3.33E-002	0	0	0
7.04E+002	2.62E+002	2.16E+003	3.16E-002	0	0	0
7.45E+002	2.64E+002	2.47E+003	3.00E-002	0	0	0
7.86E+002	2.65E+002	2.76E+003	2.85E-002	0.1	0	1
8.26E+002	2.66E+002	3.01E+003	2.82E-002	0.2	0	1
8.63E+002	2.68E+002	3.24E+003	2.81E-002	0.4	0	1
8.99E+002	2.69E+002	3.45E+003	2.79E-002	0	0	0
9.32E+002	2.70E+002	3.70E+003	2.78E-002	0	0	0
9.62E+002	2.71E+002	3.92E+003	2.78E-002	0	0	0
9.89E+002	2.71E+002	4.10E+003	2.77E-002	0	0	0
1.01E+003	2.72E+002	4.27E+003	2.77E-002	0	0	0
1.03E+003	2.73E+002	4.40E+003	2.76E-002	0	0	0
1.05E+003	2.73E+002	4.51E+003	2.76E-002			

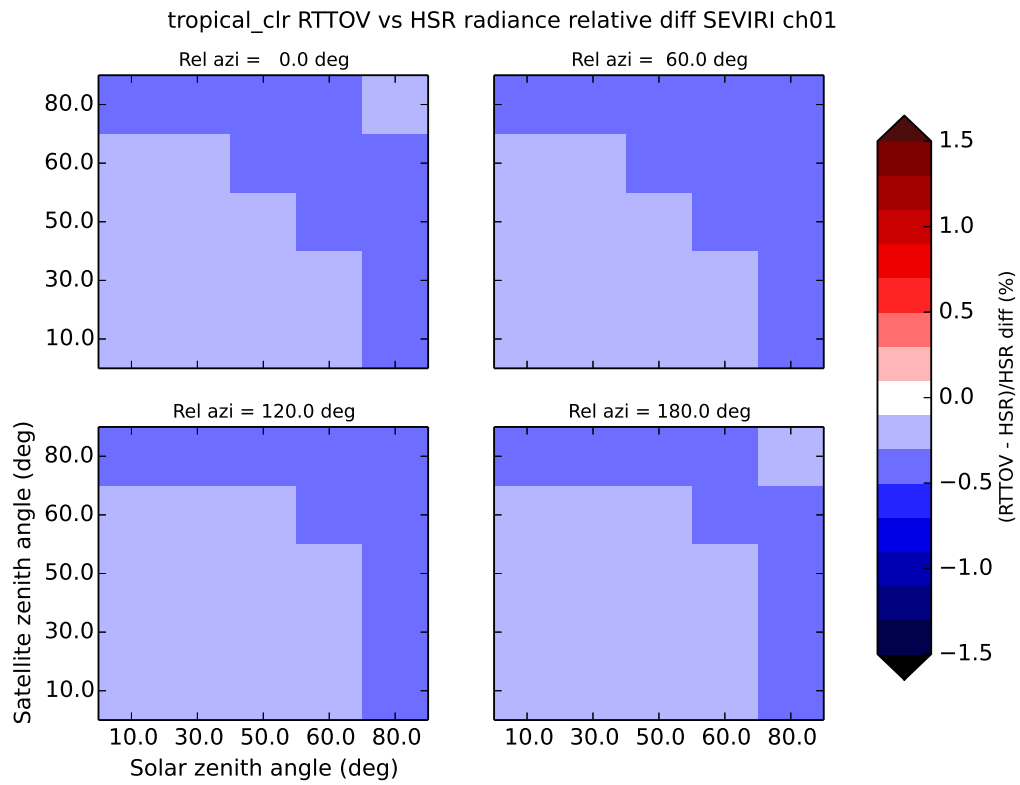


Figure 1: Tropical clear-sky profile, SEVIRI ch01, HSR vs RTTOV

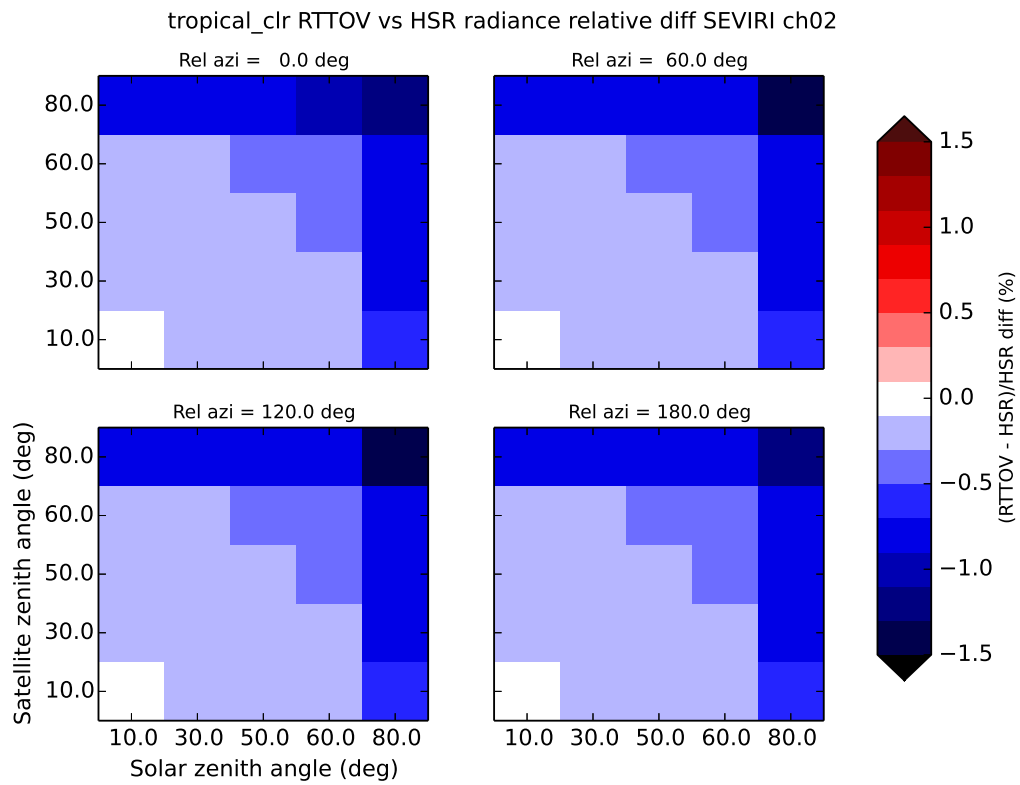


Figure 2: Tropical clear-sky profile, SEVIRI ch02, HSR vs RTTOV

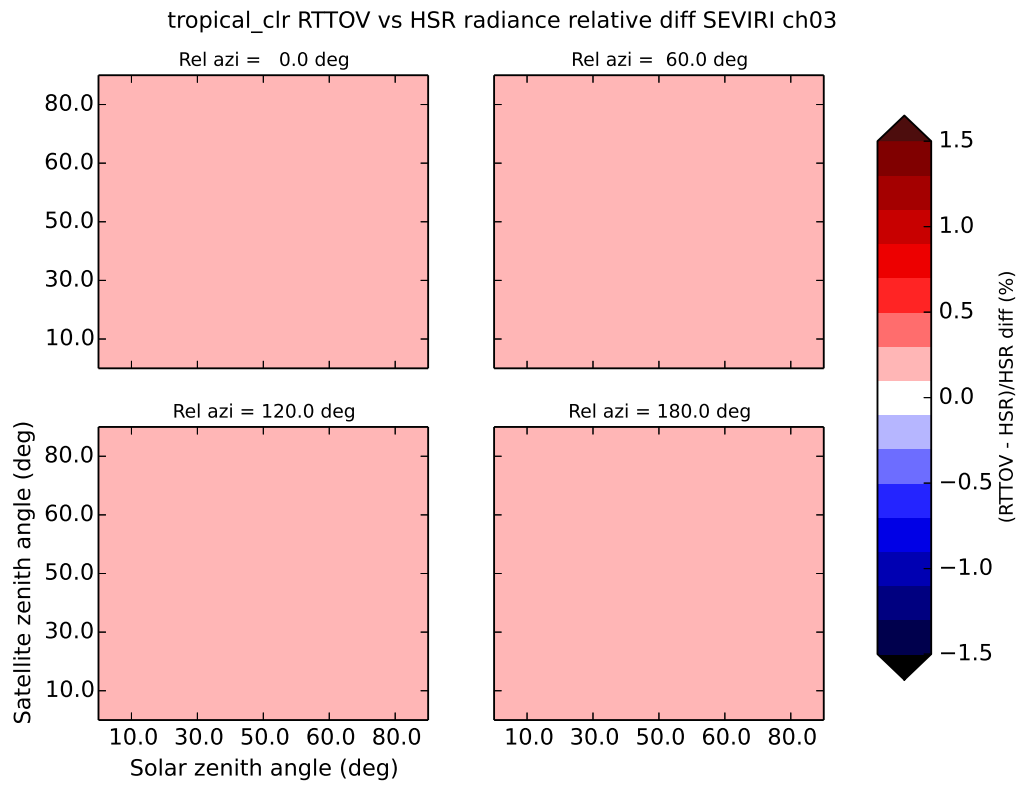


Figure 3: Tropical clear-sky profile, SEVIRI ch03, HSR vs RTTOV

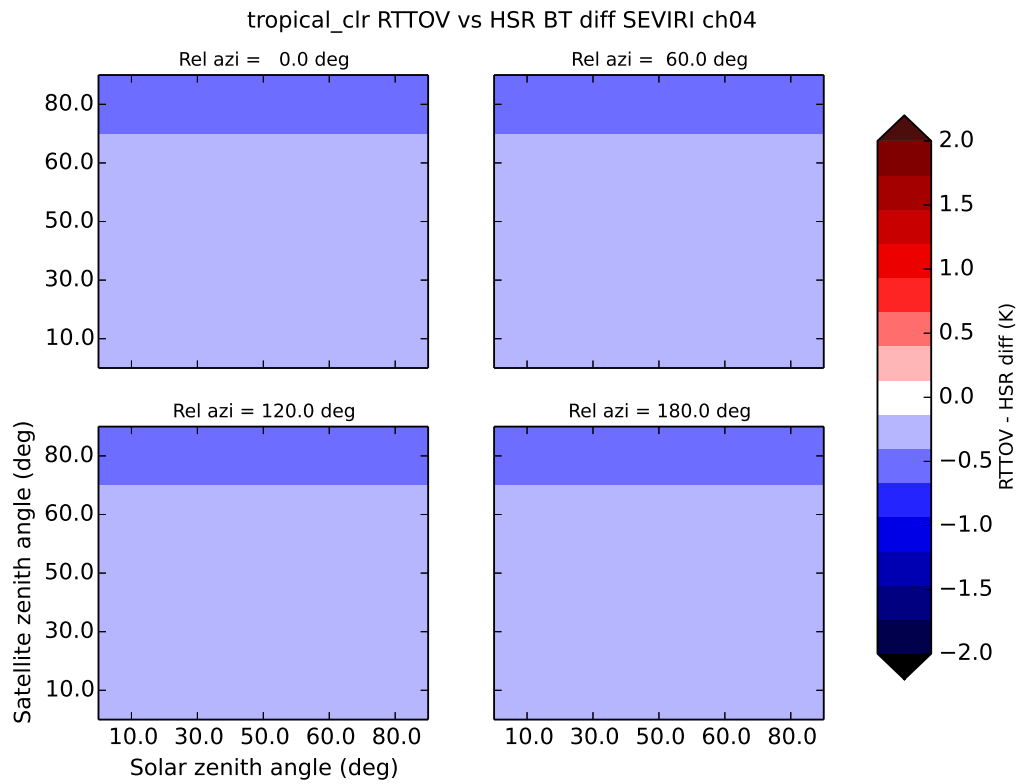


Figure 4: Tropical clear-sky profile, SEVIRI ch04, HSR vs RTTOV

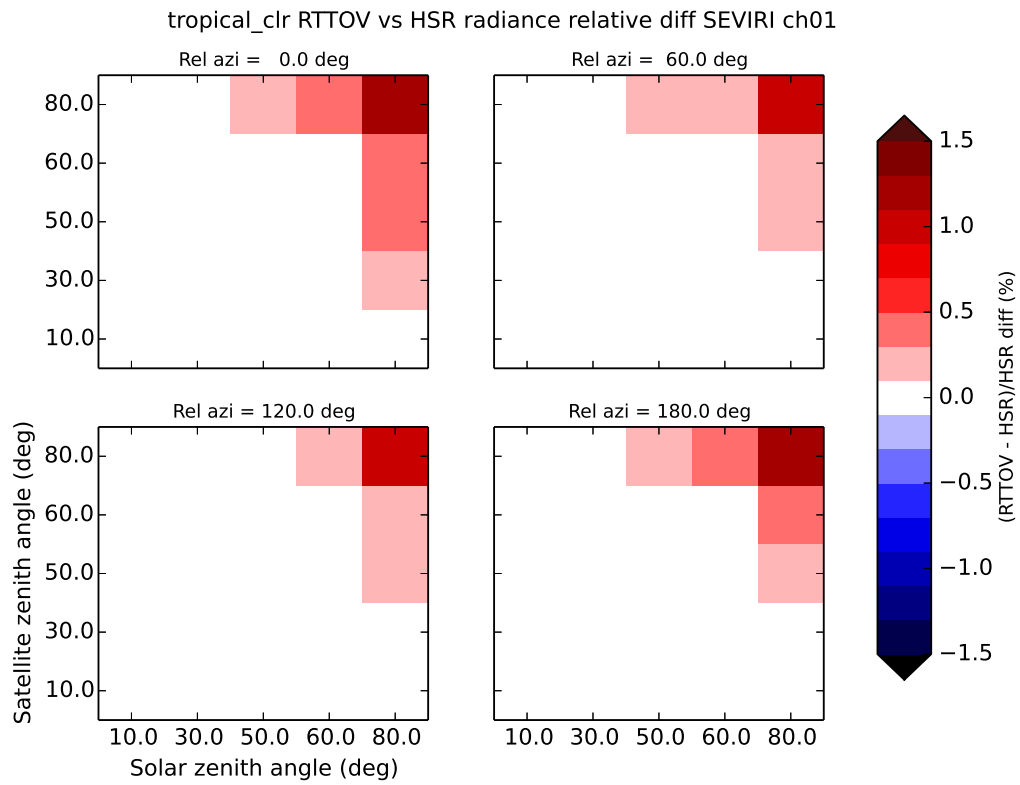


Figure 5: Tropical clear-sky profile, SEVIRI ch01, HSR vs RTTOV using Rayleigh weighted central wavenumber

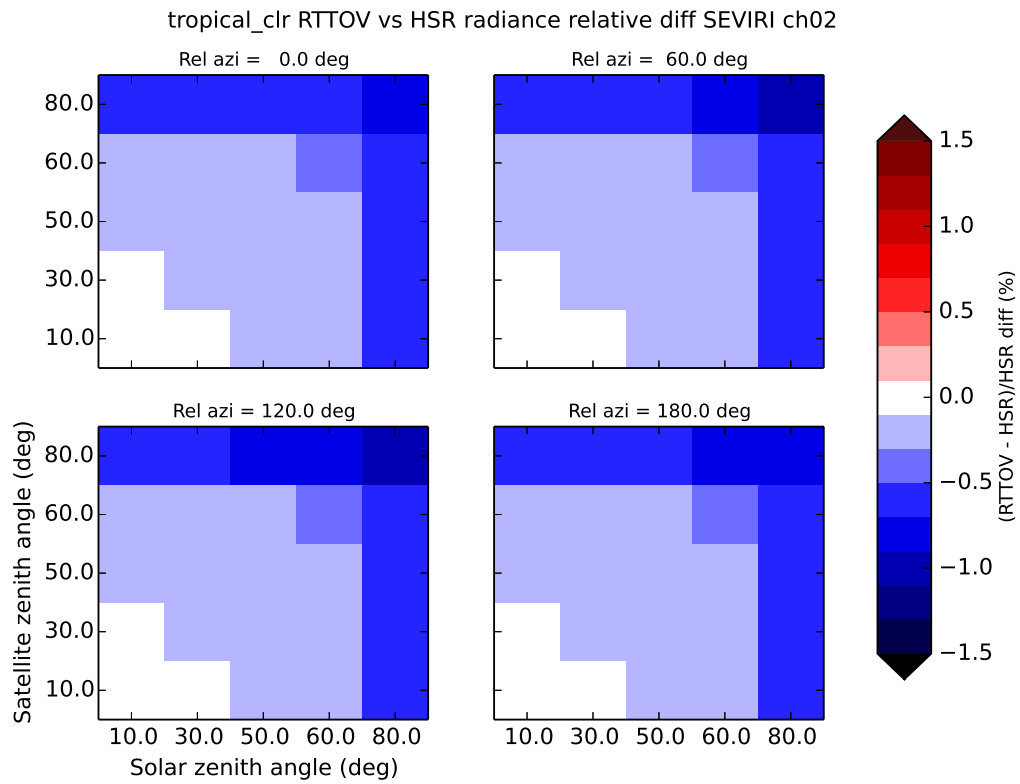


Figure 6: Tropical clear-sky profile, SEVIRI ch02, HSR vs RTTOV using Rayleigh weighted central wavenumber

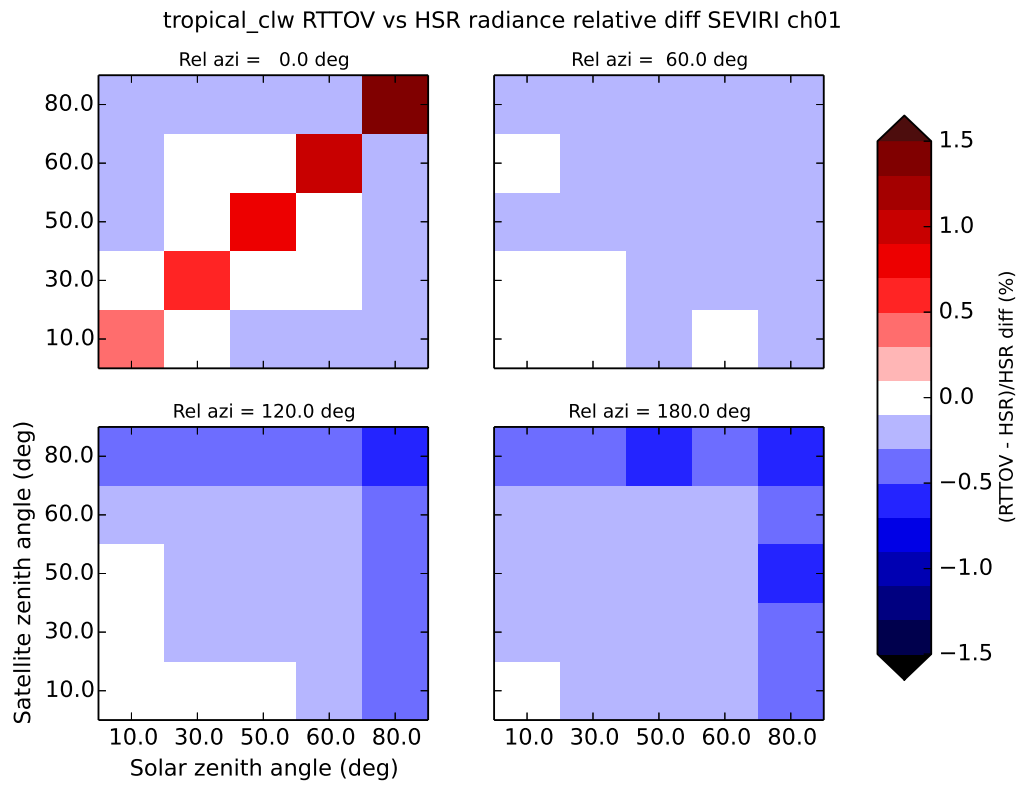


Figure 7: Tropical cloud liquid water profile, SEVIRI ch01, HSR vs RTTOV

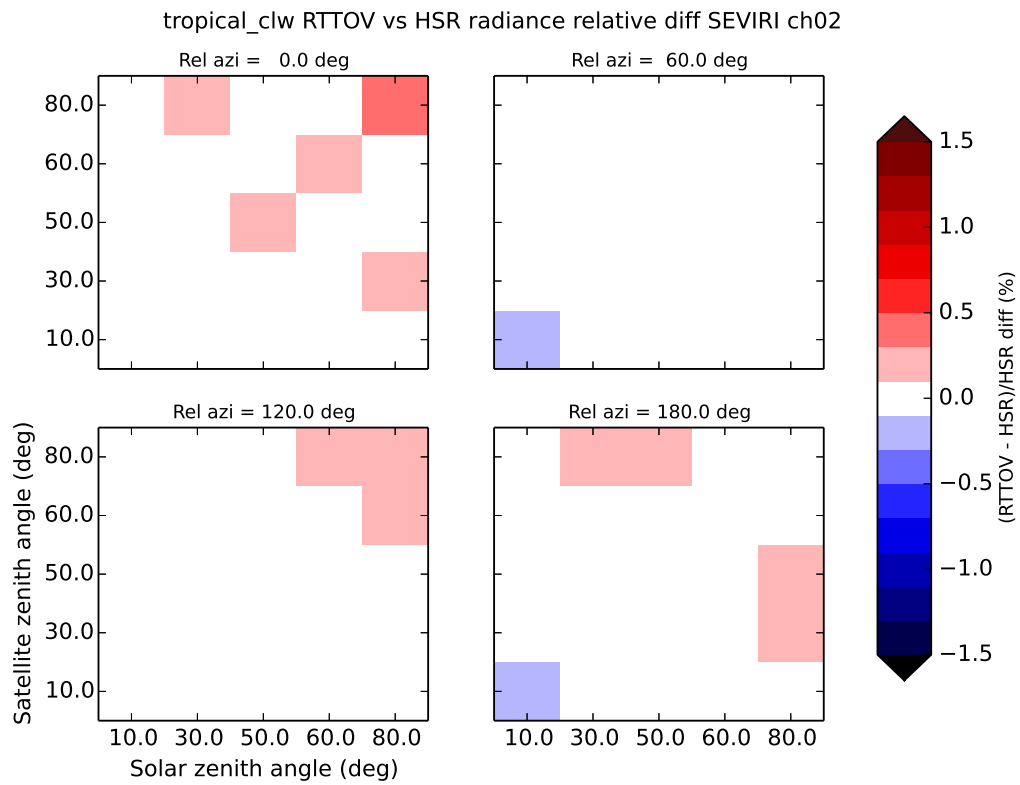


Figure 8: Tropical cloud liquid water profile, SEVIRI ch02, HSR vs RTTOV

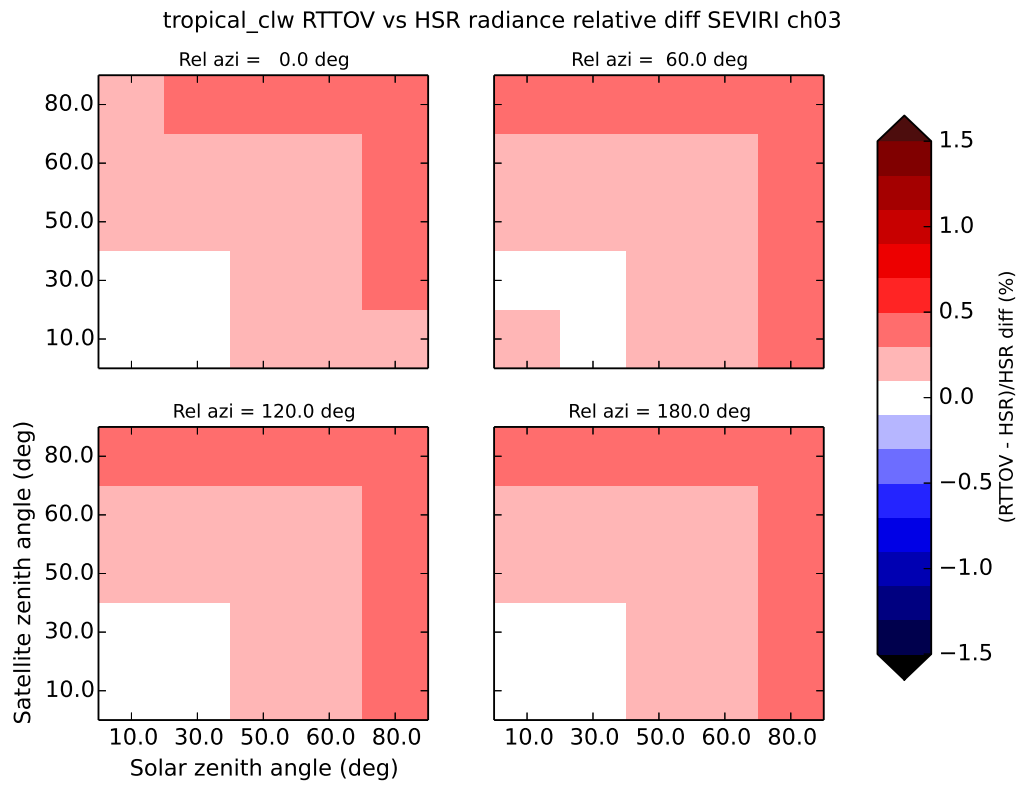


Figure 9: Tropical cloud liquid water profile, SEVIRI ch03, HSR vs RTTOV

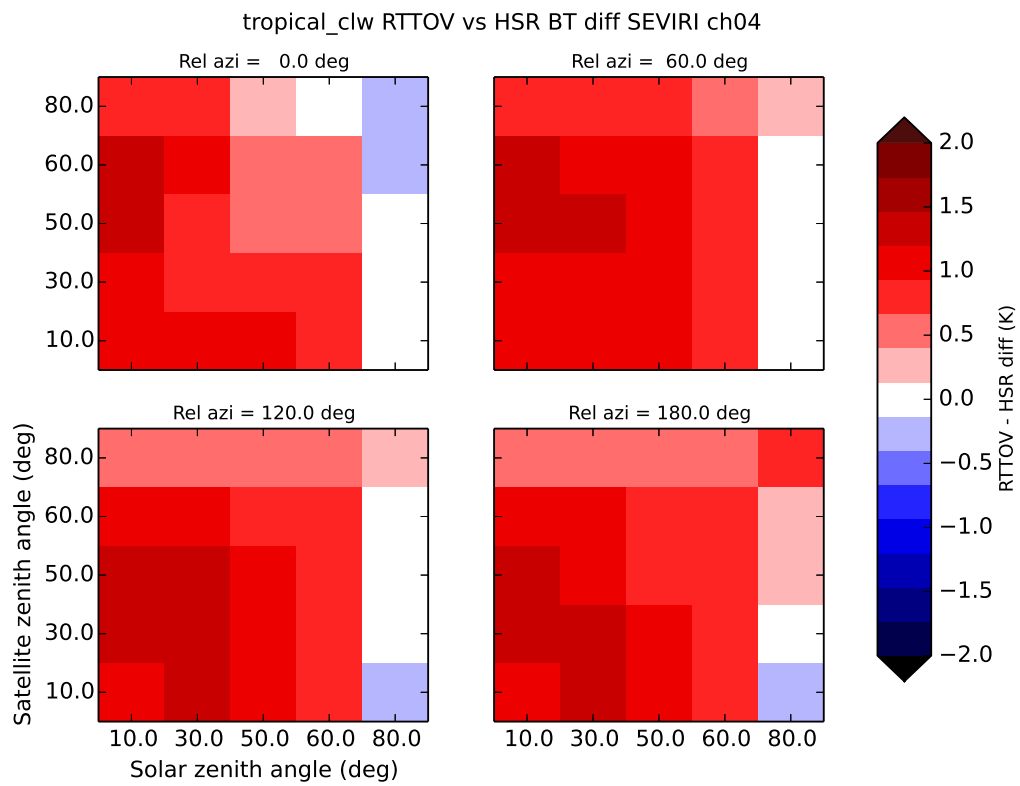


Figure 10: Tropical cloud liquid water profile, SEVIRI ch04, HSR vs RTTOV

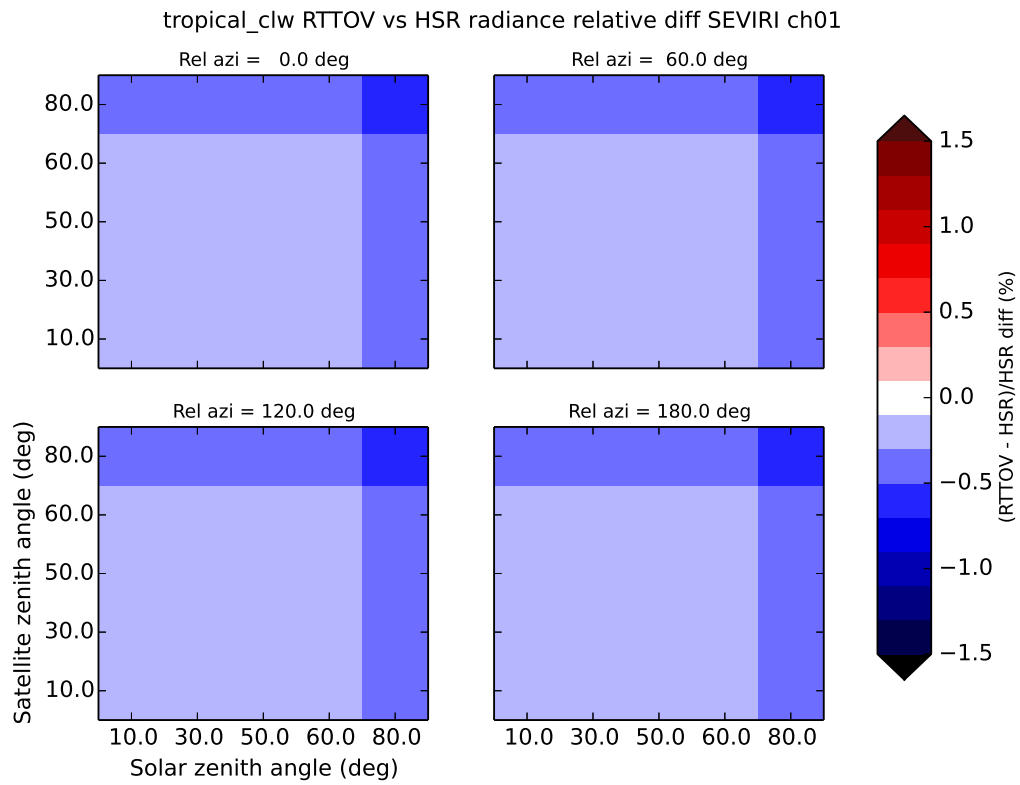


Figure 11: Tropical cloud liquid water profile, SEVIRI ch01, HSR vs RTTOV using channel-averaged cloud properties

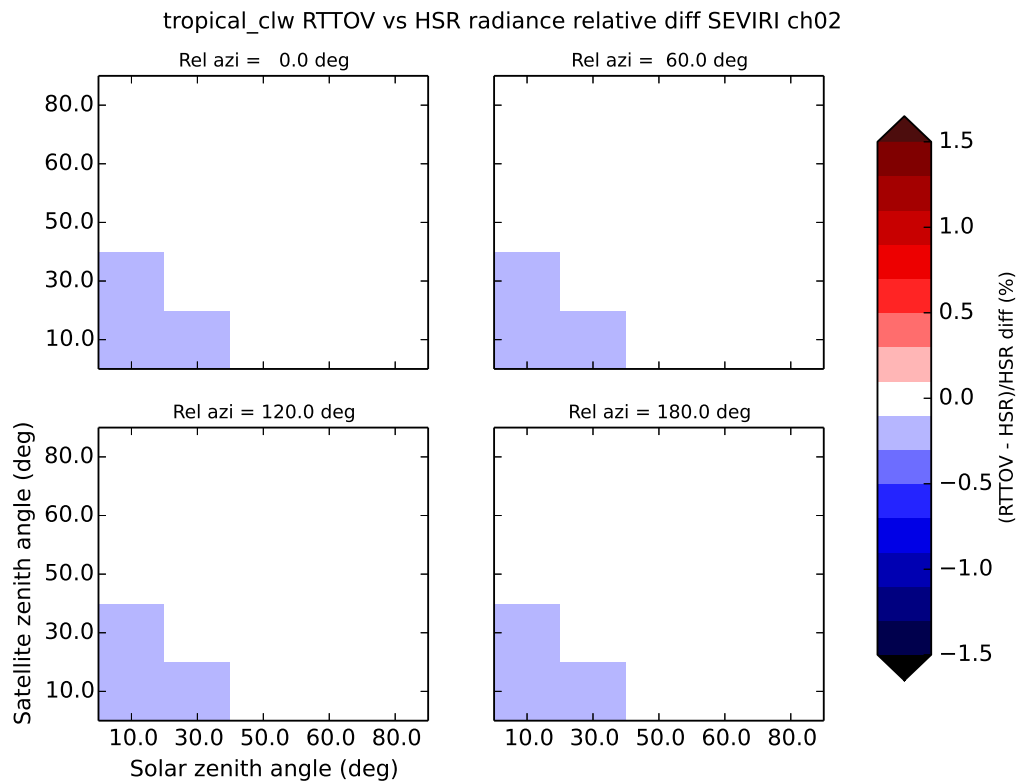


Figure 12: Tropical cloud liquid water profile, SEVIRI ch02, HSR vs RTTOV using channel-averaged cloud properties

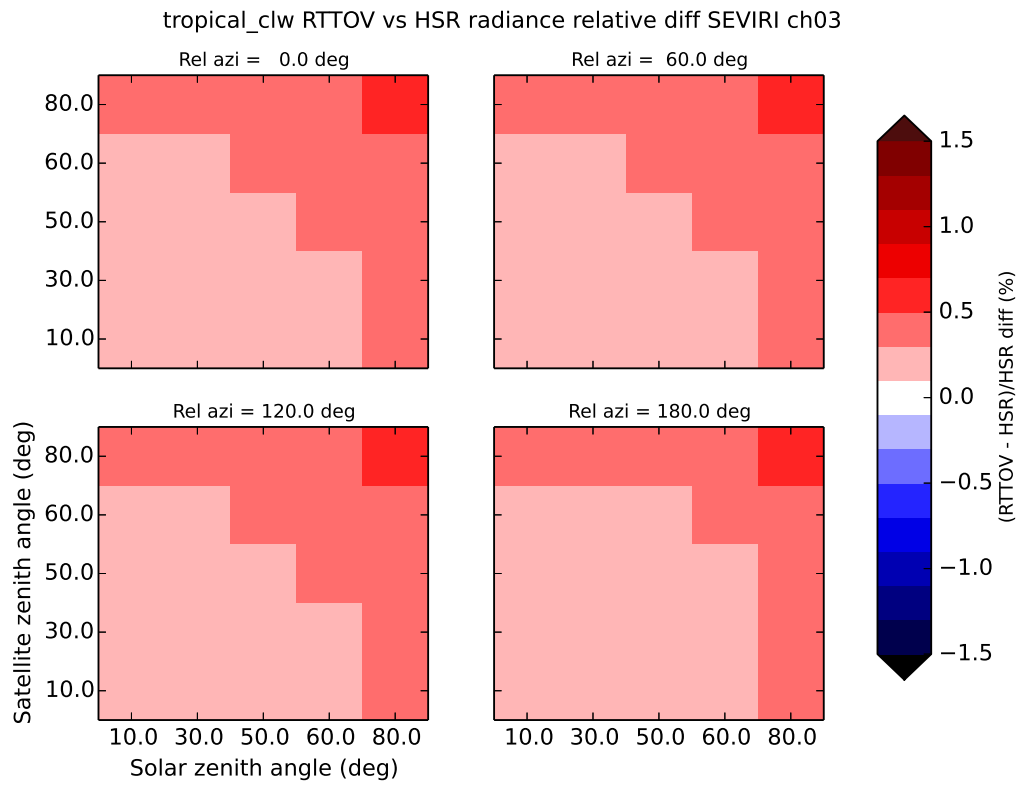


Figure 13: Tropical cloud liquid water profile, SEVIRI ch03, HSR vs RTTOV using channel-averaged cloud properties

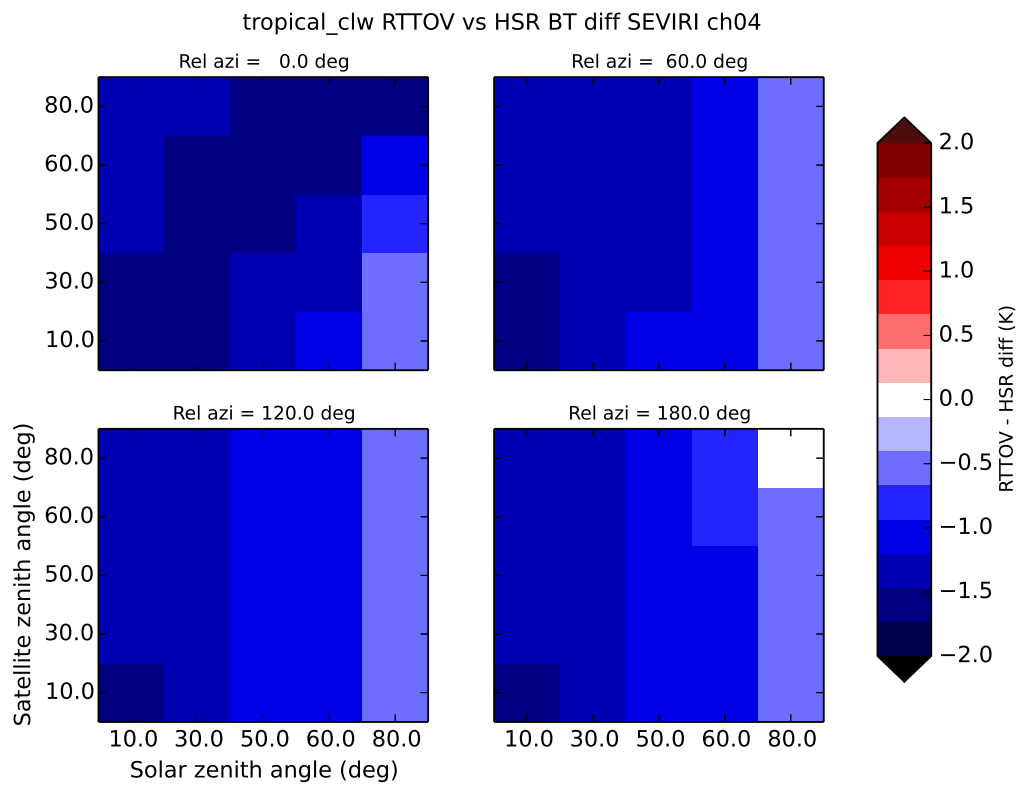


Figure 14: Tropical cloud liquid water profile, SEVIRI ch04, HSR vs RTTOV using channel-averaged cloud properties



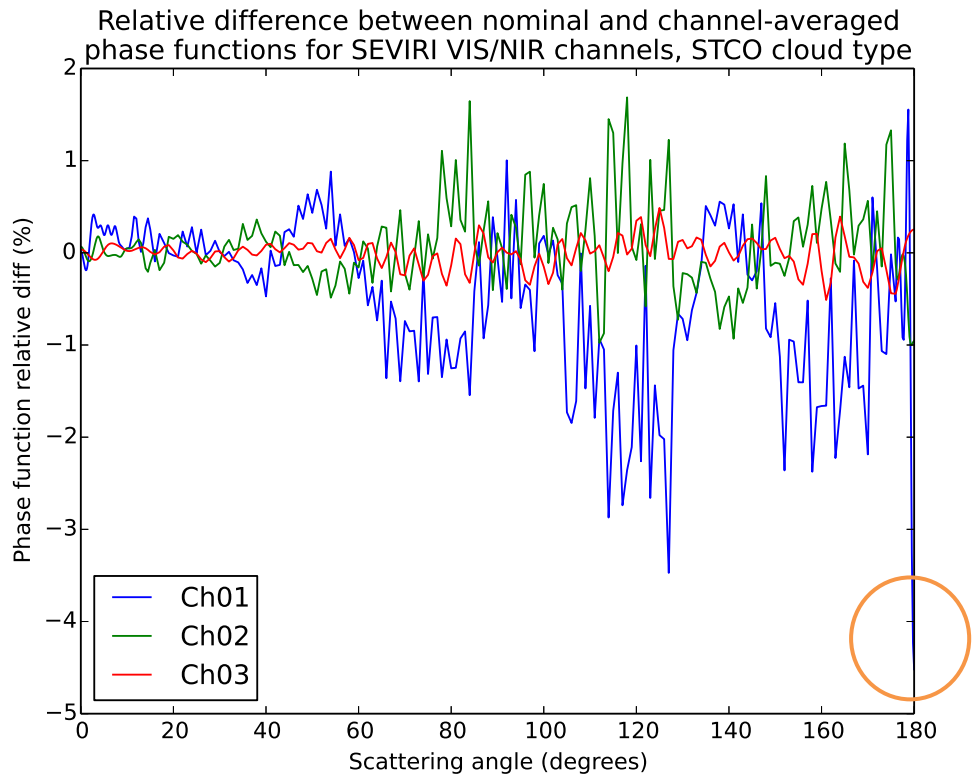


Figure 15: relative difference of channel-averaged phase function minus phase function at nominal channel wavenumber for SEVIRI visible/near-IR channels for the STCO cloud liquid water particle

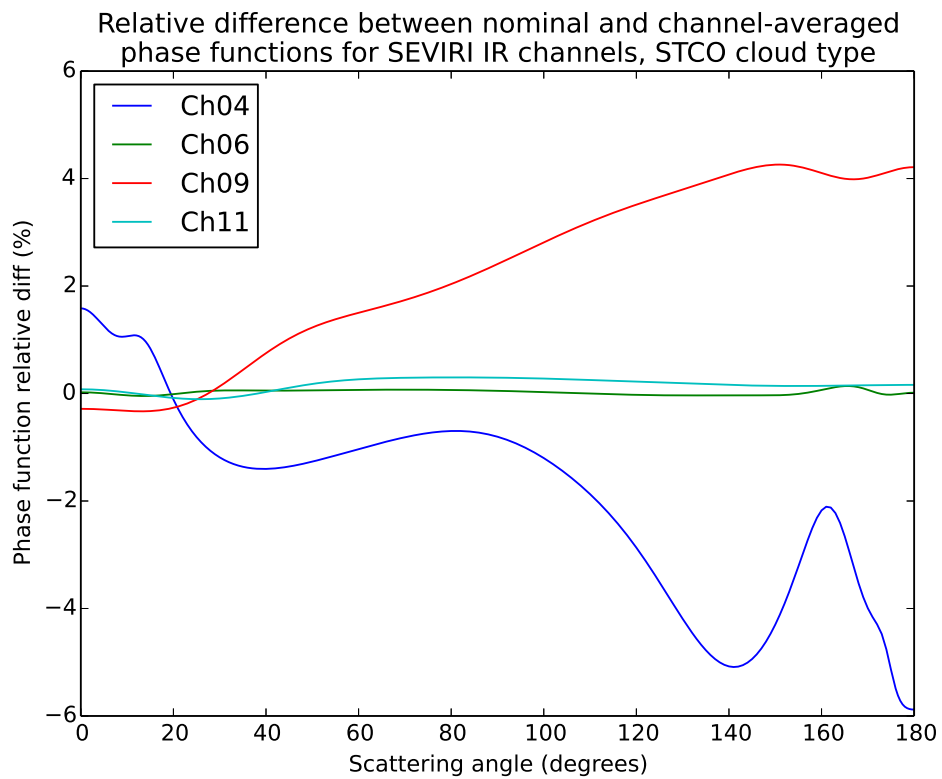


Figure 16: relative difference of channel-averaged phase function minus phase function at nominal channel wavenumber for SEVIRI IR channels for the STCO cloud liquid water particle

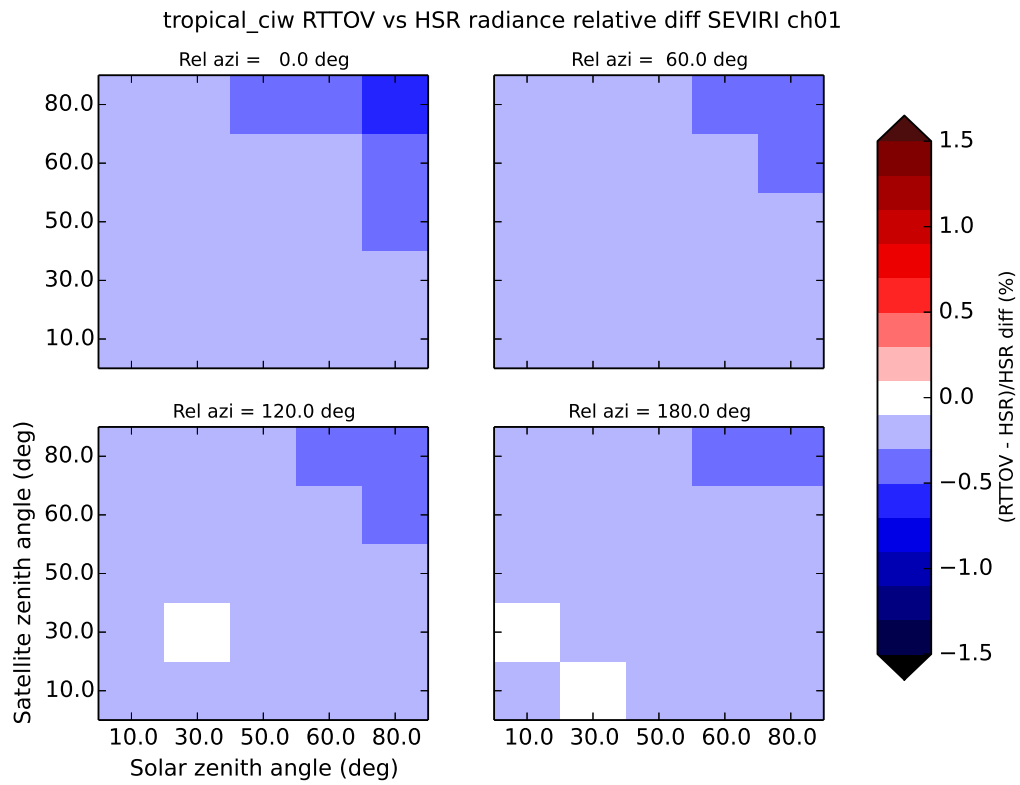


Figure 17: Tropical cloud ice water profile, SEVIRI ch01, HSR vs RTTOV

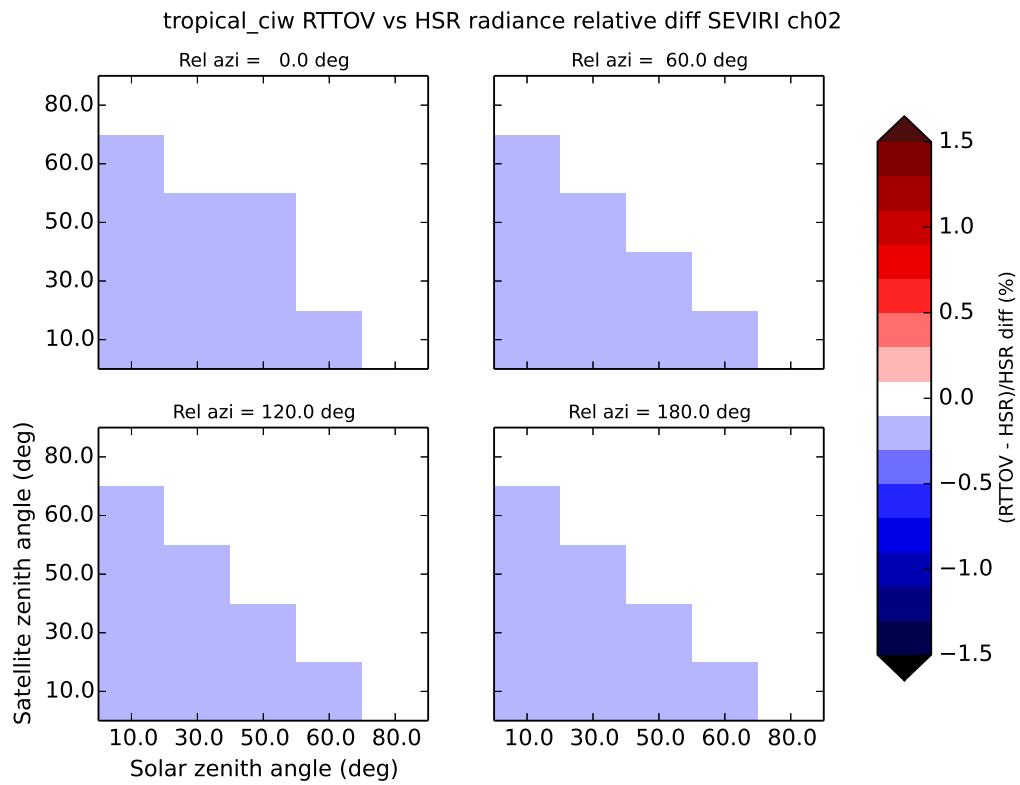


Figure 18: Tropical cloud ice water profile, SEVIRI ch02, HSR vs RTTOV

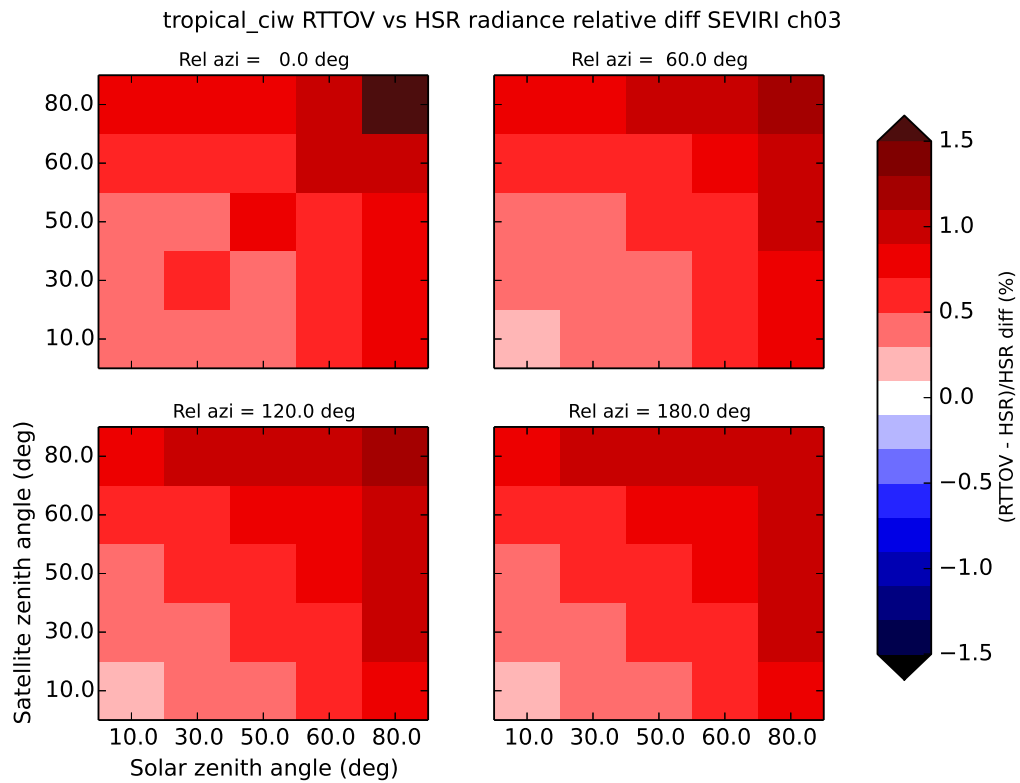


Figure 19: Tropical cloud ice water profile, SEVIRI ch03, HSR vs RTTOV (largest absolute difference is less than 1.7%)

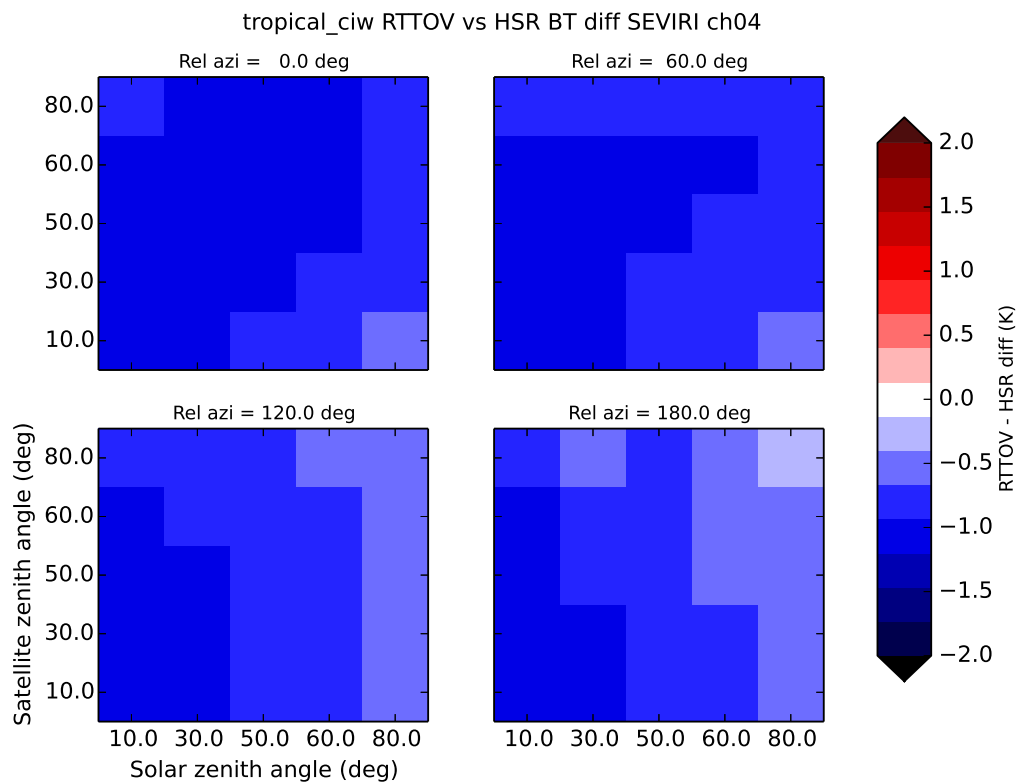


Figure 20: Tropical cloud ice water profile, SEVIRI ch04, HSR vs RTTOV

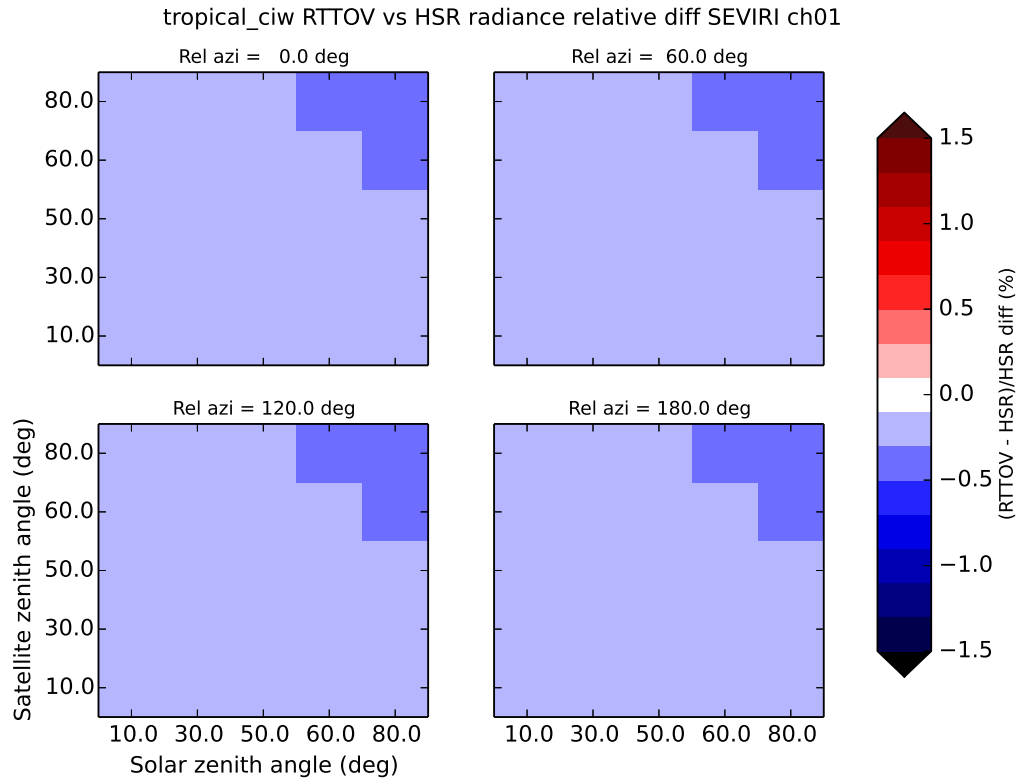


Figure 21: Tropical cloud ice water profile, SEVIRI ch01, HSR vs RTTOV using channel-averaged cloud properties

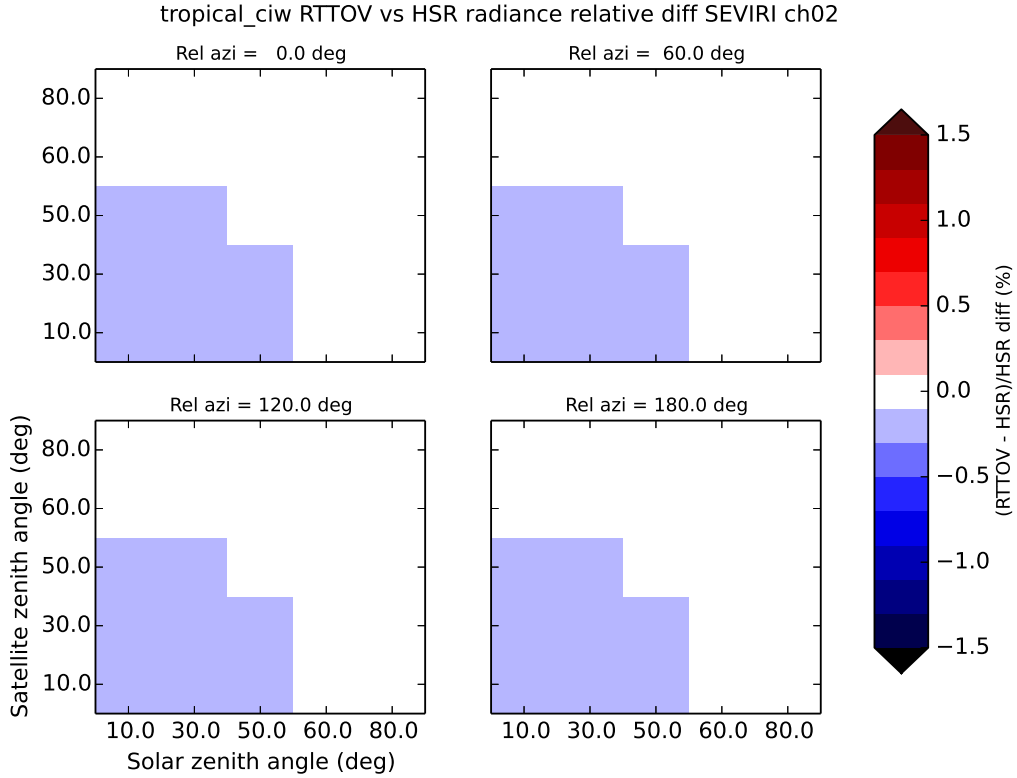


Figure 22: Tropical cloud ice water profile, SEVIRI ch02, HSR vs RTTOV using channel-averaged cloud properties

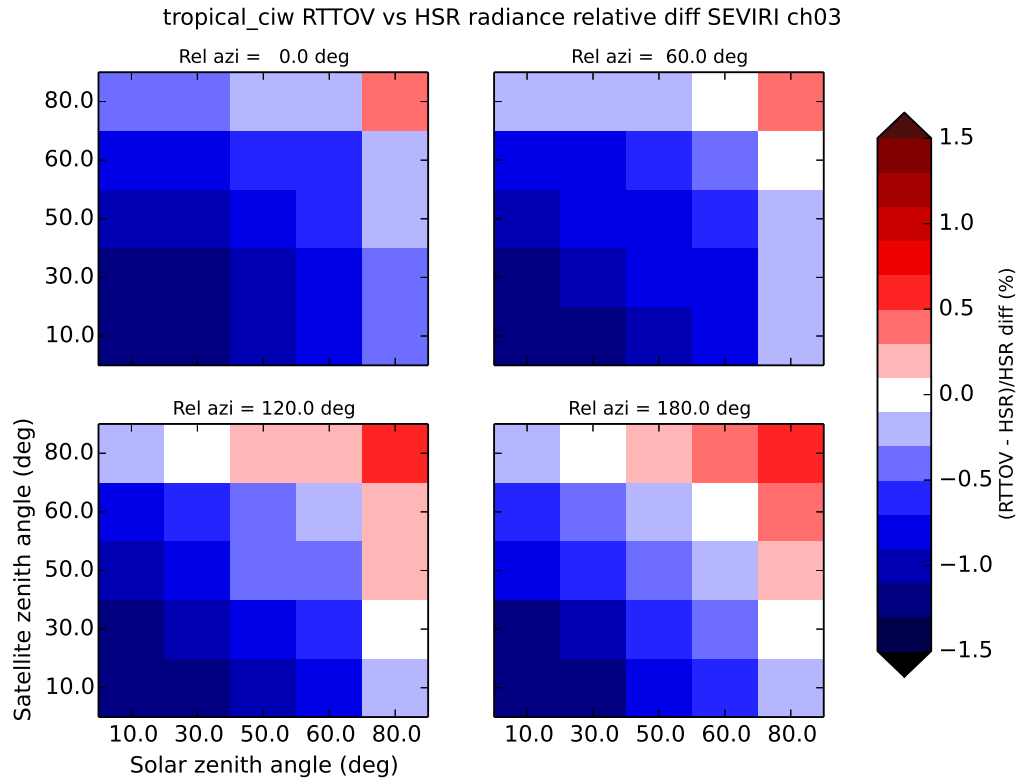


Figure 23: Tropical cloud ice water profile, SEVIRI ch03, HSR vs RTTOV using channel-averaged cloud properties

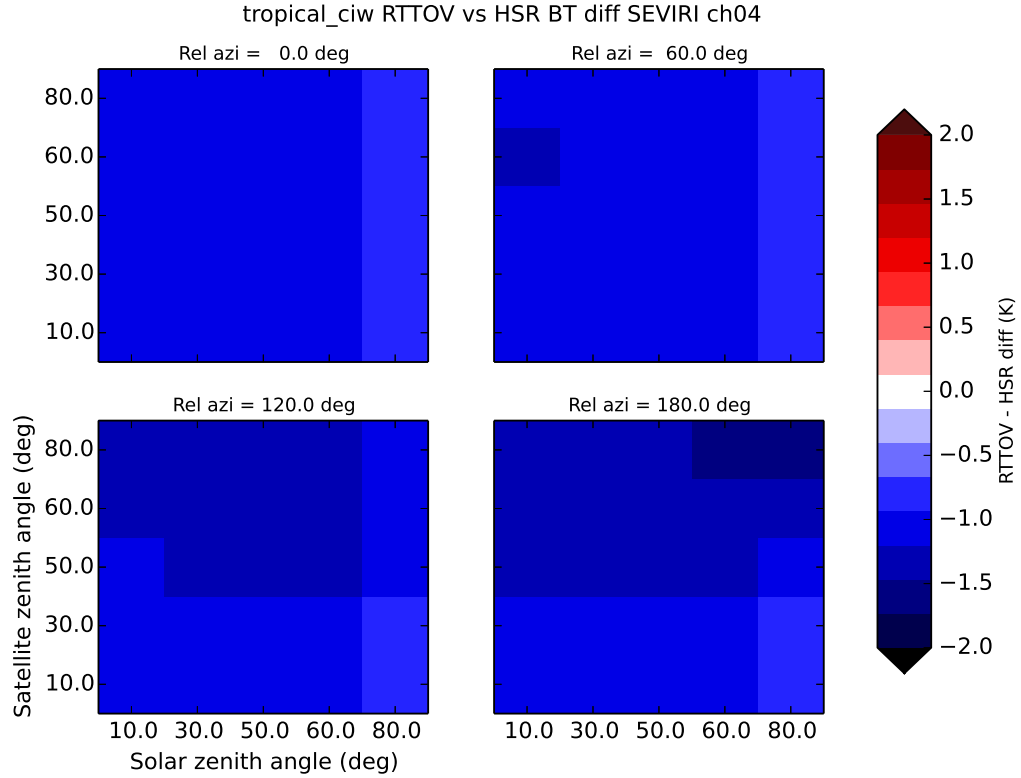


Figure 24: Tropical cloud ice water profile, SEVIRI ch04, HSR vs RTTOV using channel-averaged cloud properties

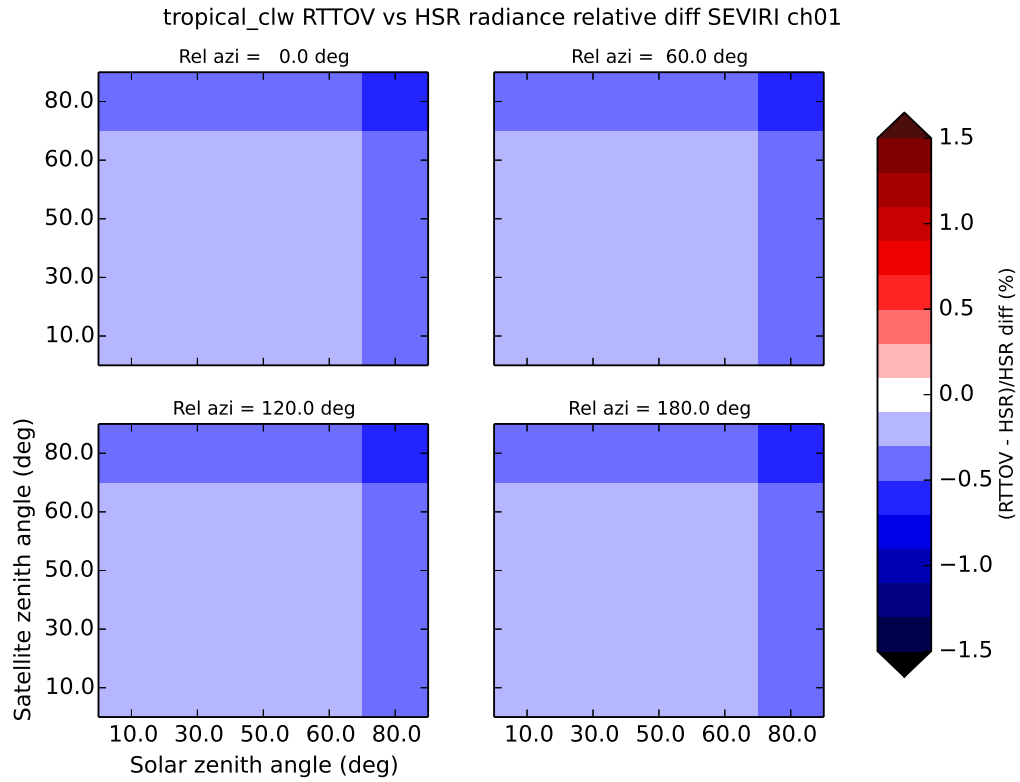


Figure 25: Tropical cloud liquid water profile, SEVIRI ch01, HSR with fixed cloud optical properties vs RTTOV

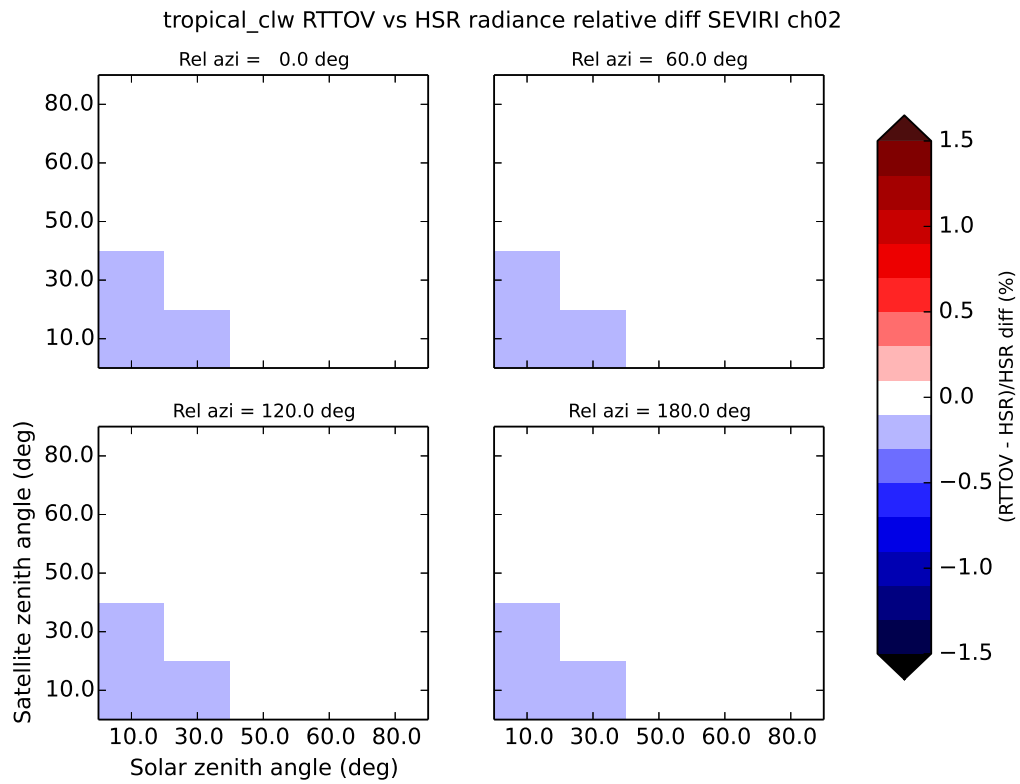


Figure 26: Tropical cloud liquid water profile, SEVIRI ch02, HSR with fixed cloud optical properties vs RTTOV

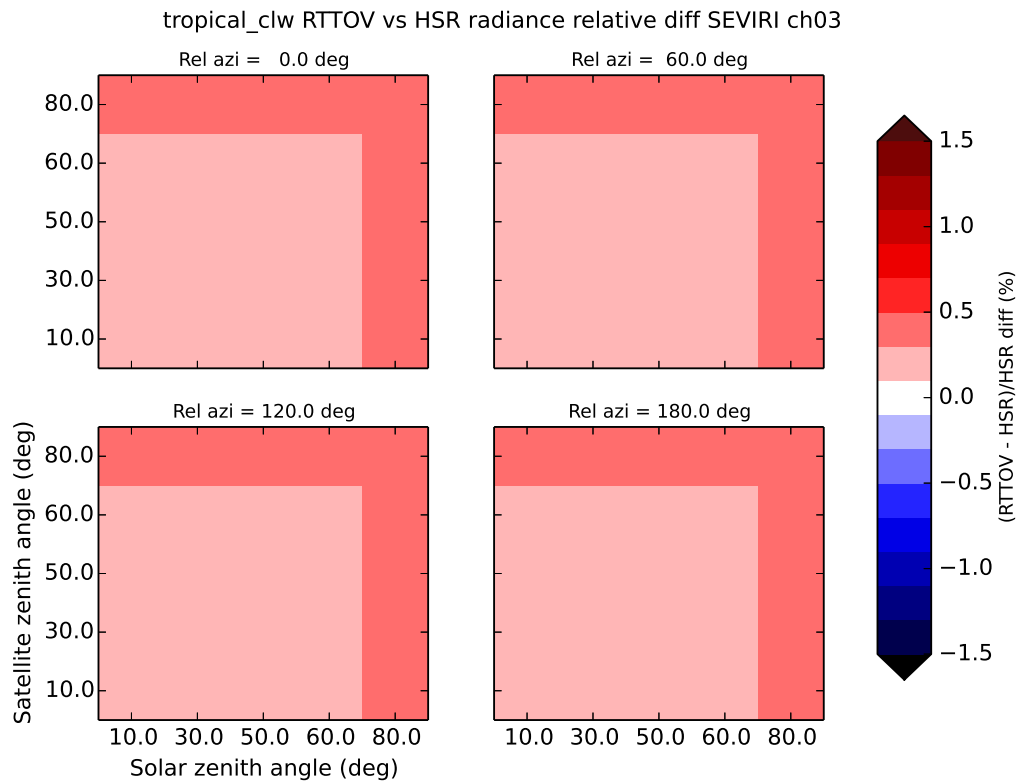


Figure 27: Tropical cloud liquid water profile, SEVIRI ch03, HSR with fixed cloud optical properties vs RTTOV

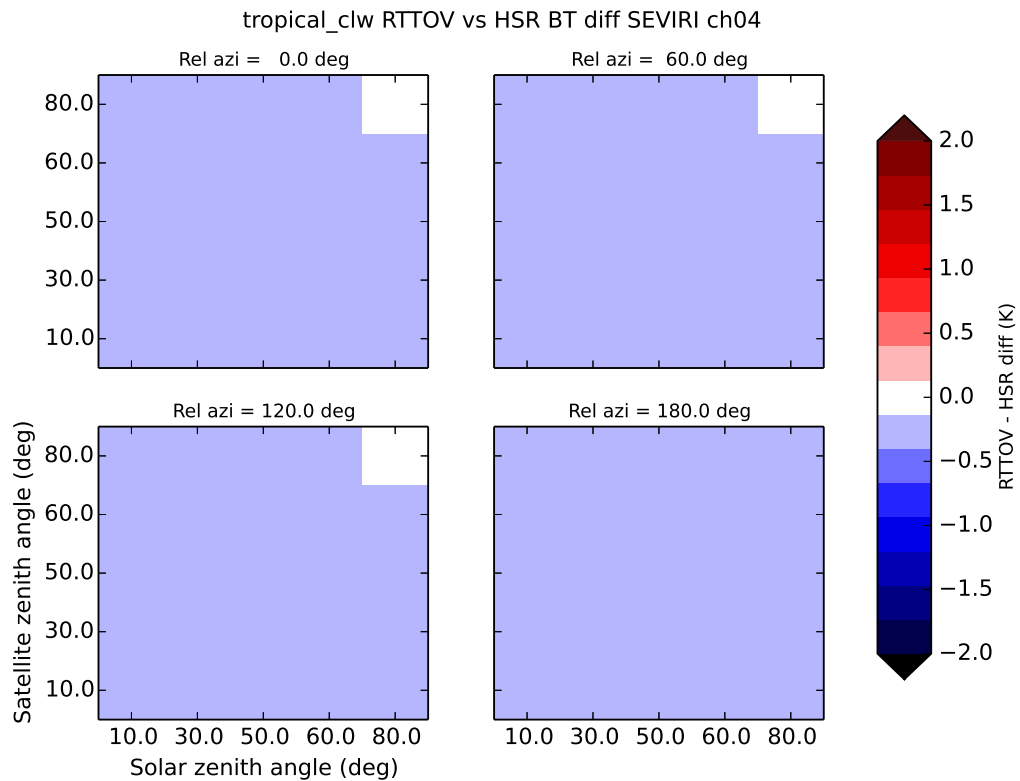


Figure 28: Tropical cloud liquid water profile, SEVIRI ch04, HSR with fixed cloud optical properties vs RTTOV

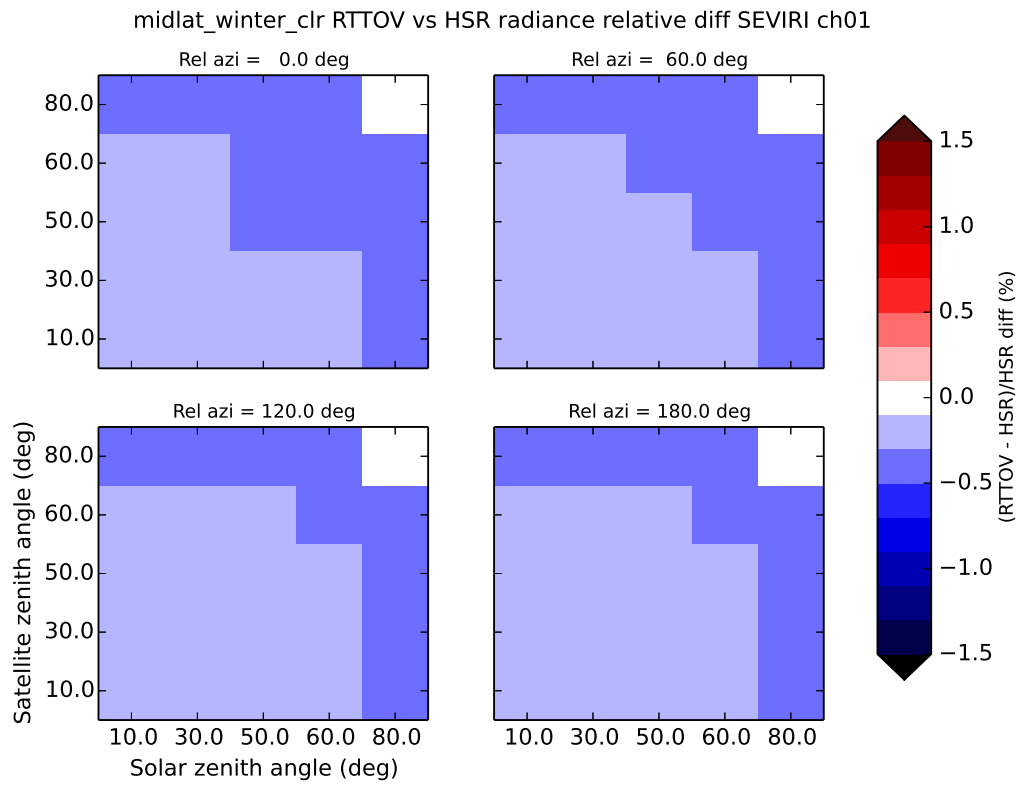


Figure 29: Mid-latitude winter clear-sky profile, SEVIRI ch01, HSR vs RTTOV

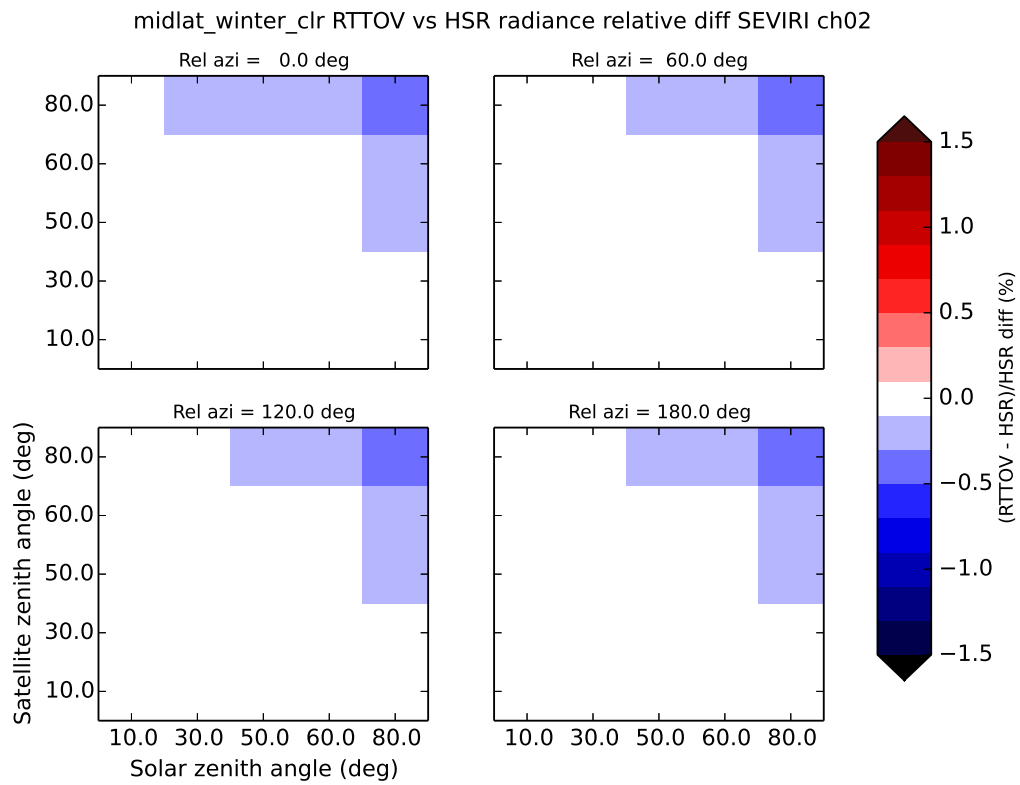


Figure 30: Mid-latitude winter clear-sky profile, SEVIRI ch02, HSR vs RTTOV



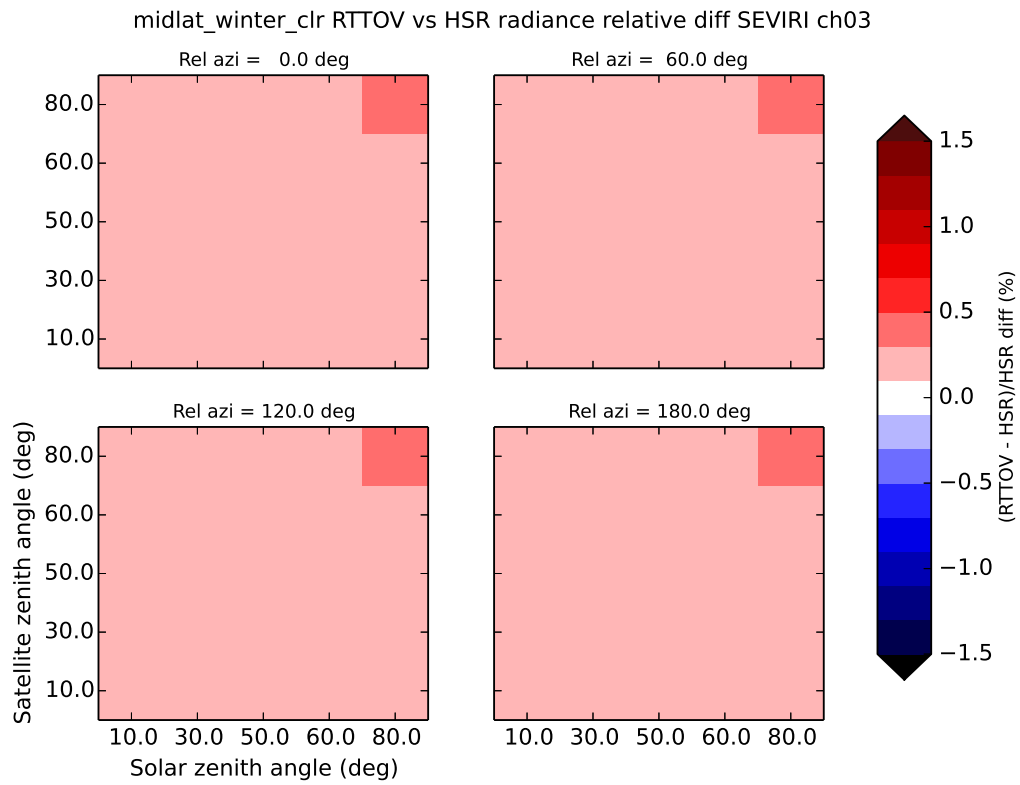


Figure 31: Mid-latitude winter clear-sky profile, SEVIRI ch03, HSR vs RTTOV

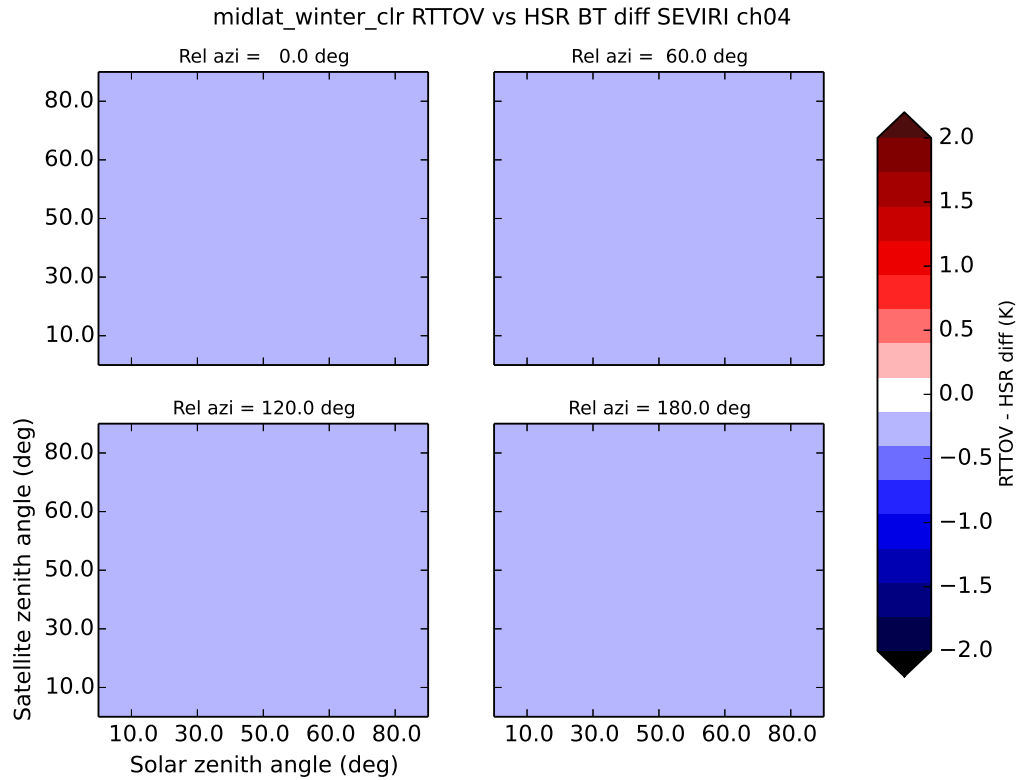


Figure 32: Mid-latitude winter clear-sky profile, SEVIRI ch04, HSR vs RTTOV

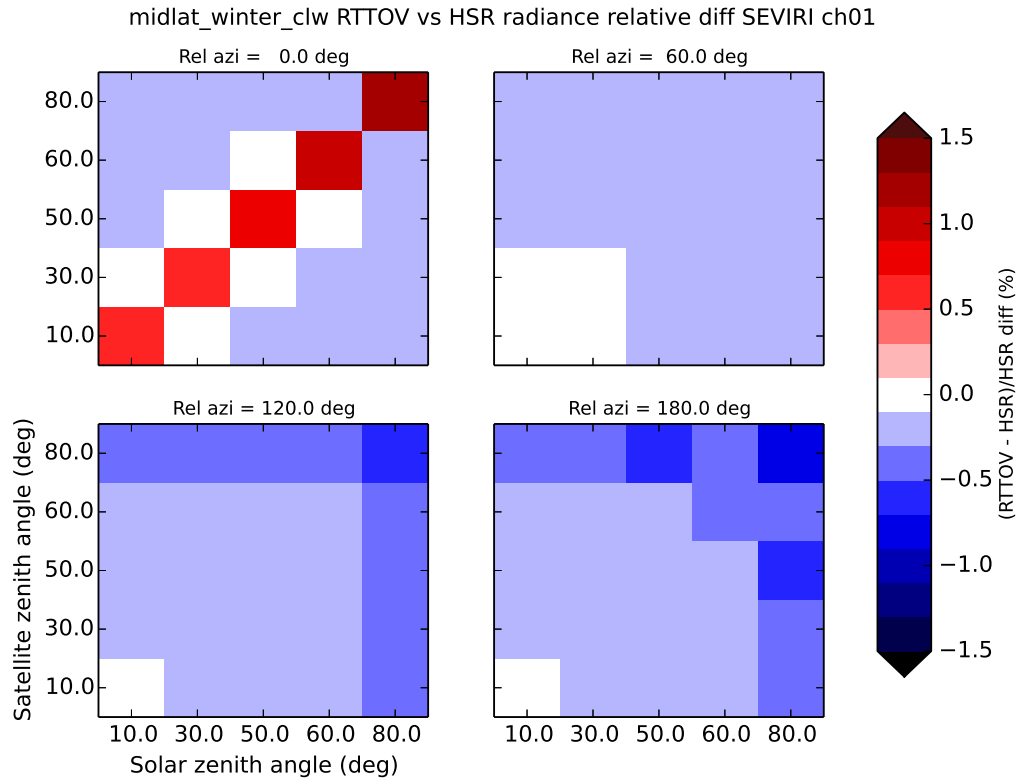


Figure 33: Mid-latitude winter cloud liquid water profile, SEVIRI ch01, HSR vs RTTOV

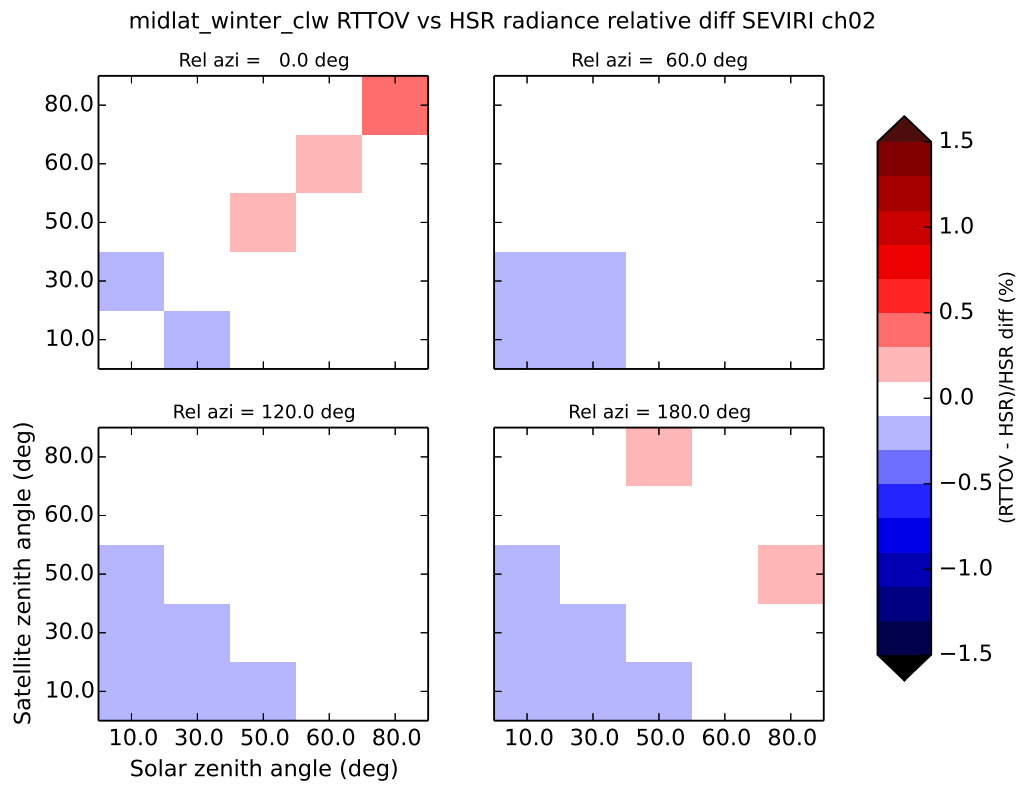


Figure 34: Mid-latitude winter cloud liquid water profile, SEVIRI ch02, HSR vs RTTOV

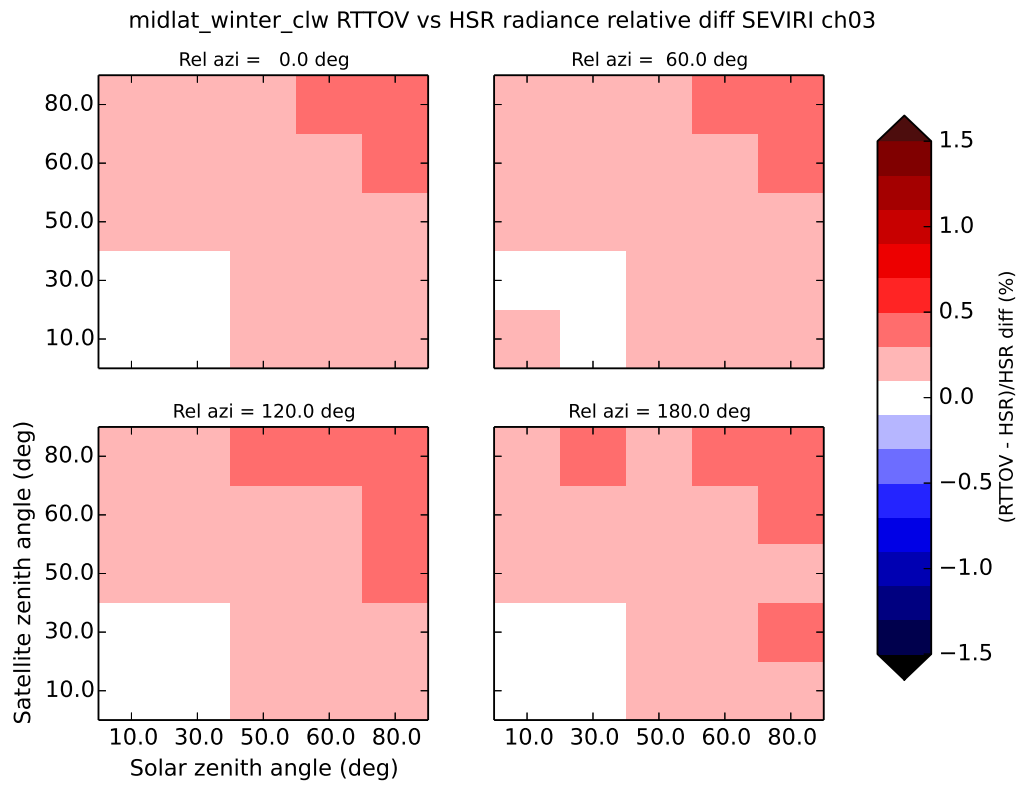


Figure 35: Mid-latitude winter cloud liquid water profile, SEVIRI ch03, HSR vs RTTOV

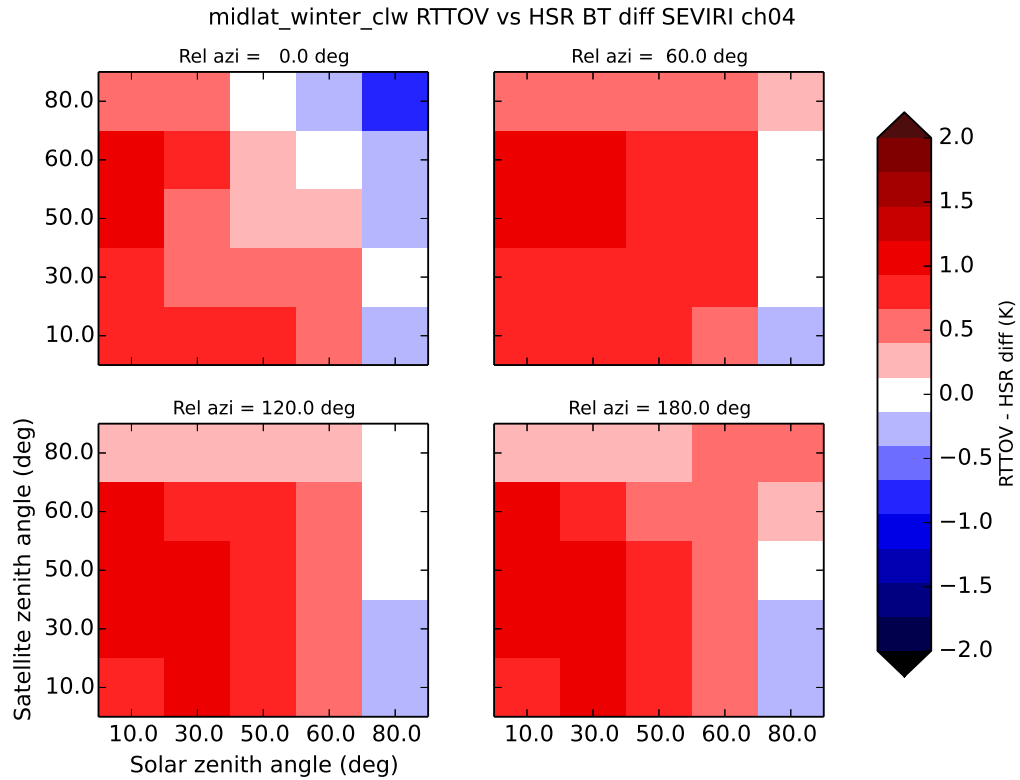


Figure 36: Mid-latitude winter cloud liquid water profile, SEVIRI ch04, HSR vs RTTOV

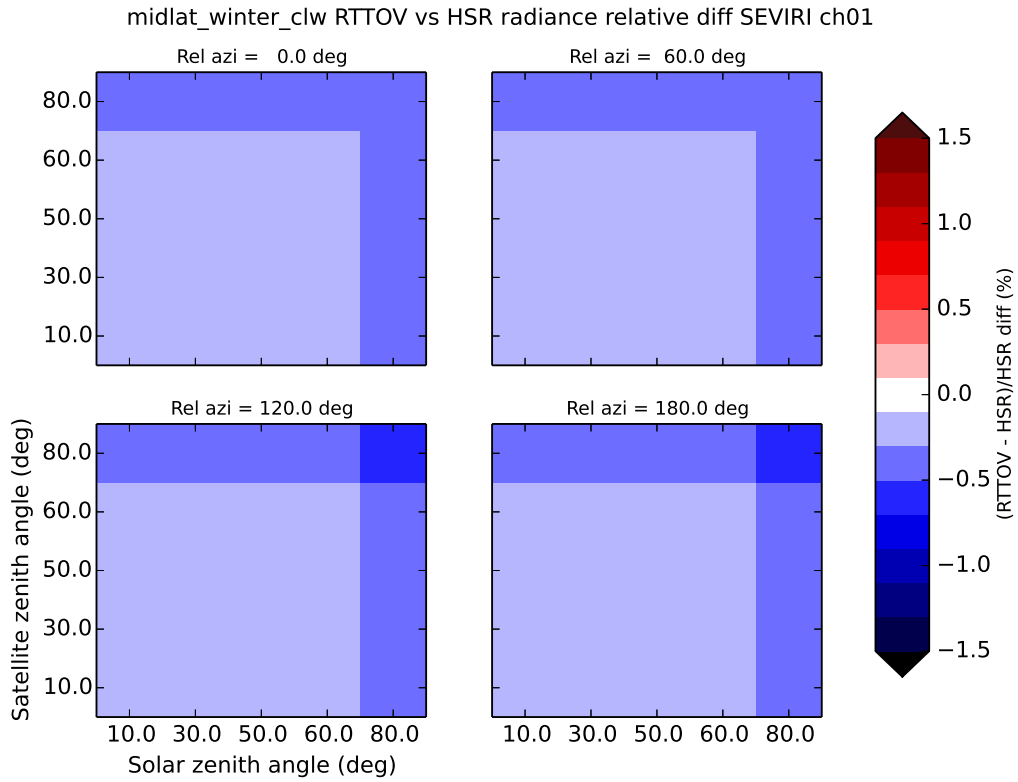


Figure 37: Mid-latitude winter cloud liquid water profile, SEVIRI ch01, HSR vs RTTOV using channel-averaged cloud properties

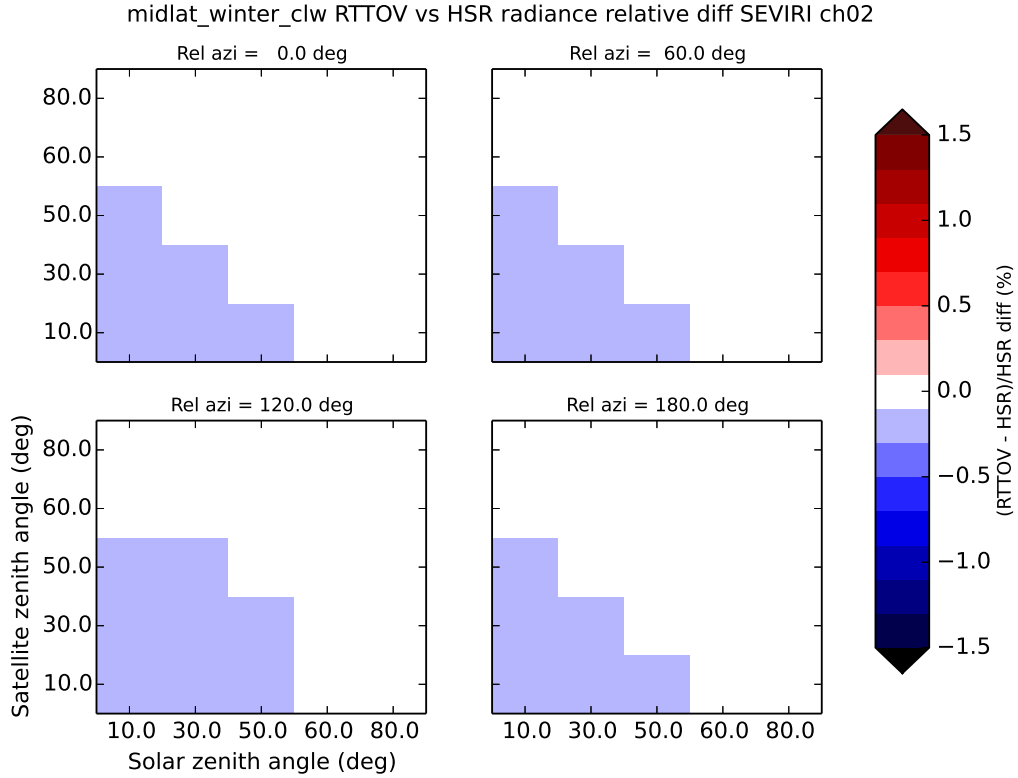


Figure 38: Mid-latitude winter cloud liquid water profile, SEVIRI ch02, HSR vs RTTOV using channel-averaged cloud properties

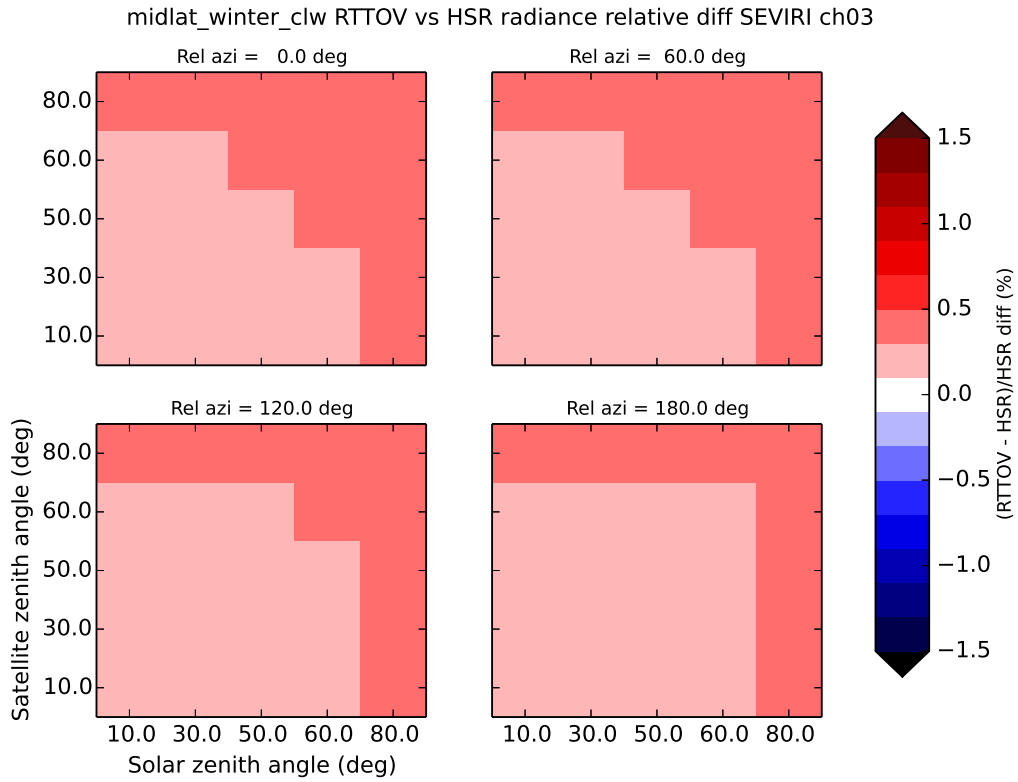


Figure 39: Mid-latitude winter cloud liquid water profile, SEVIRI ch03, HSR vs RTTOV using channel-averaged cloud properties

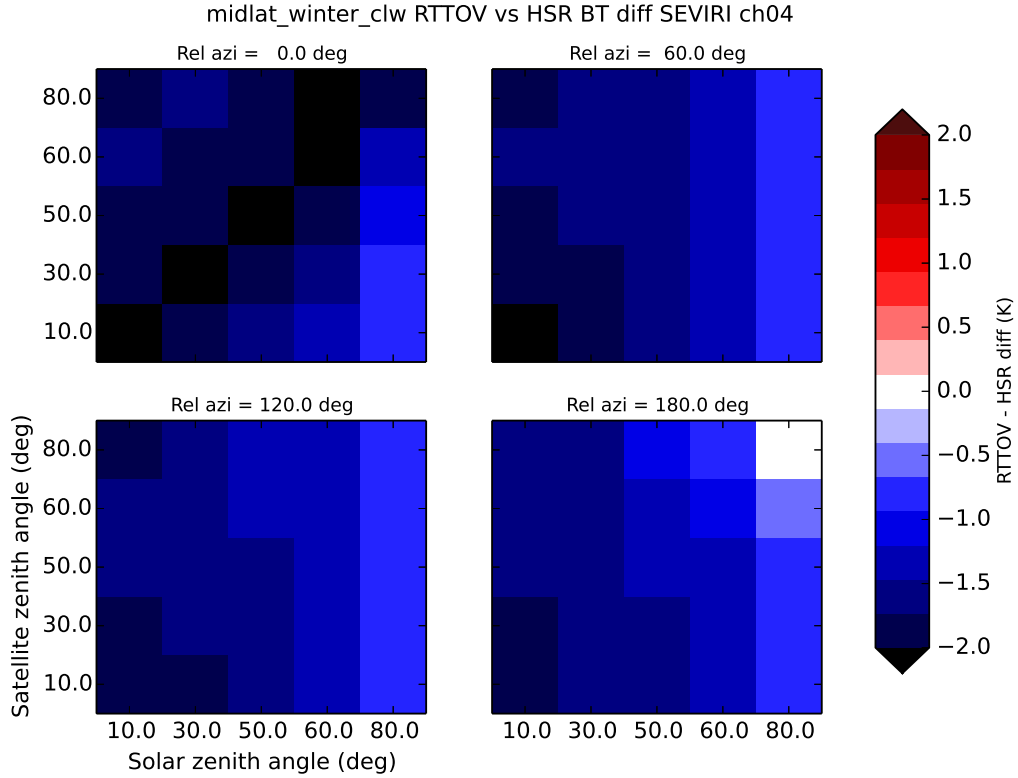


Figure 40: Mid-latitude winter cloud liquid water profile, SEVIRI ch04, HSR vs RTTOV using channel-averaged cloud properties (largest absolute differences are less than 2.1K)

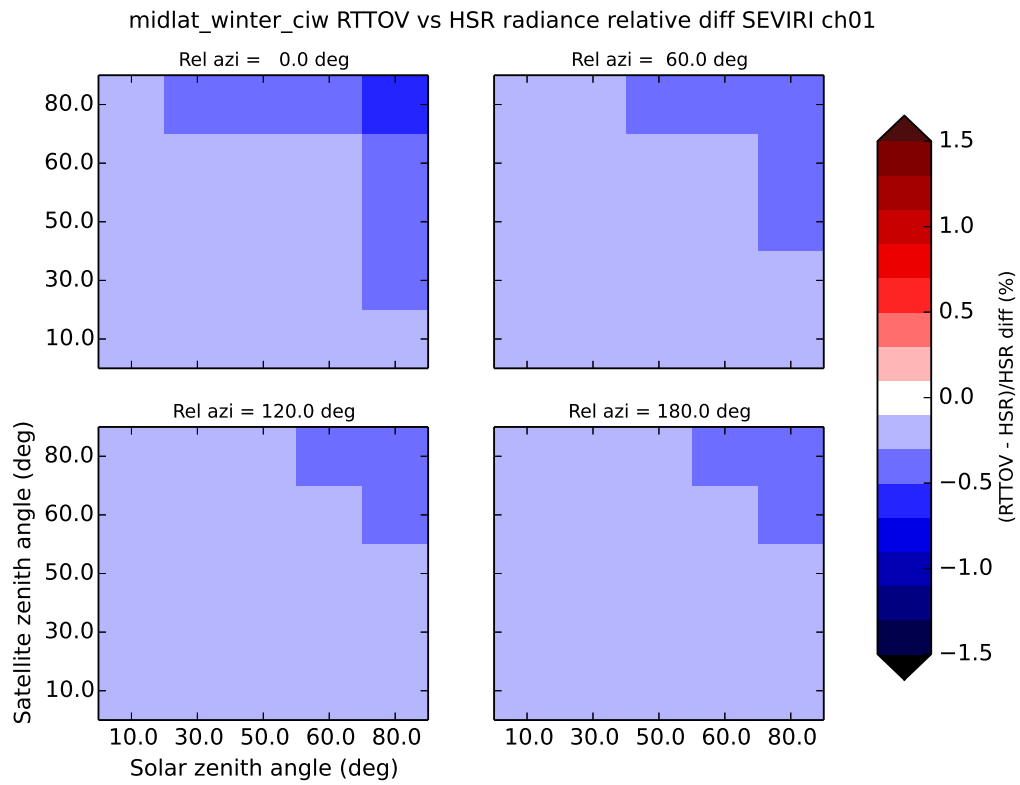


Figure 41: Mid-latitude winter cloud ice water profile, SEVIRI ch01, HSR vs RTTOV

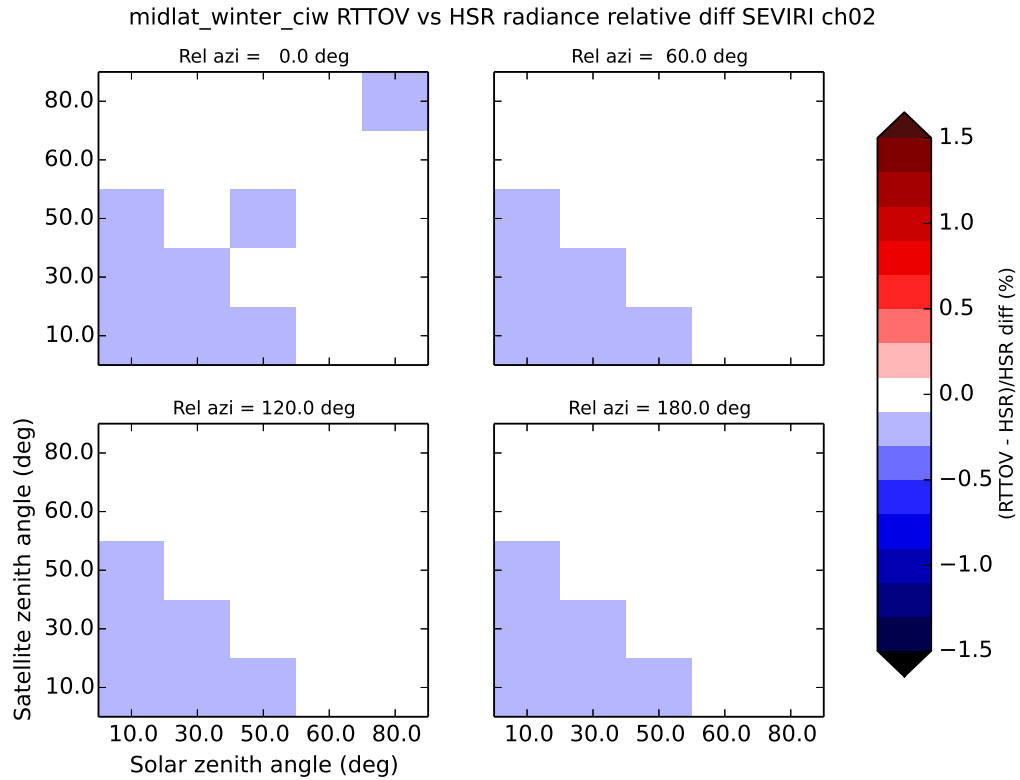


Figure 41: Mid-latitude winter cloud ice water profile, SEVIRI ch02, HSR vs RTTOV

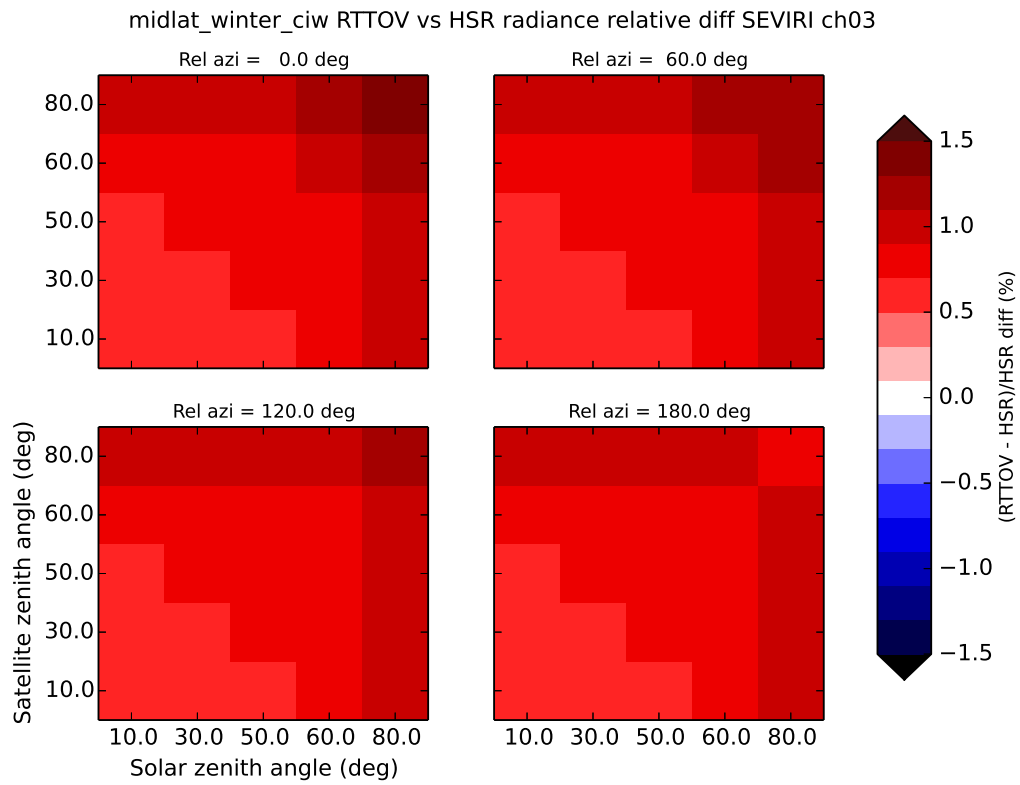


Figure 43: Mid-latitude winter cloud ice water profile, SEVIRI ch03, HSR vs RTTOV

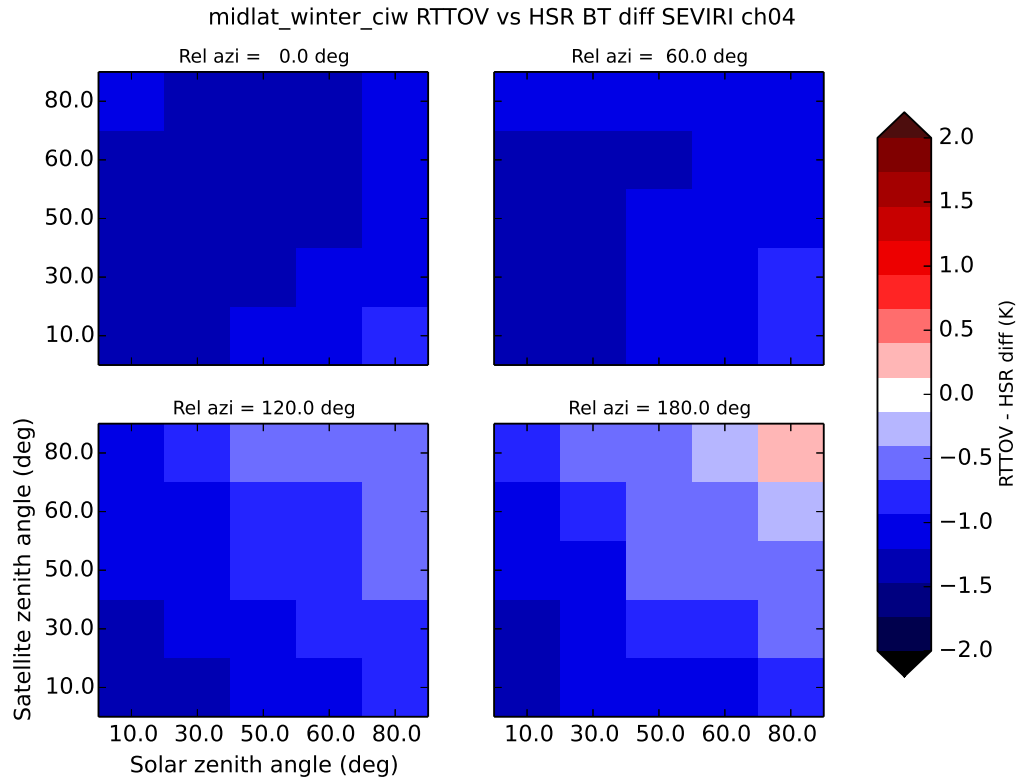


Figure 44: Mid-latitude winter cloud ice water profile, SEVIRI ch04, HSR vs RTTOV

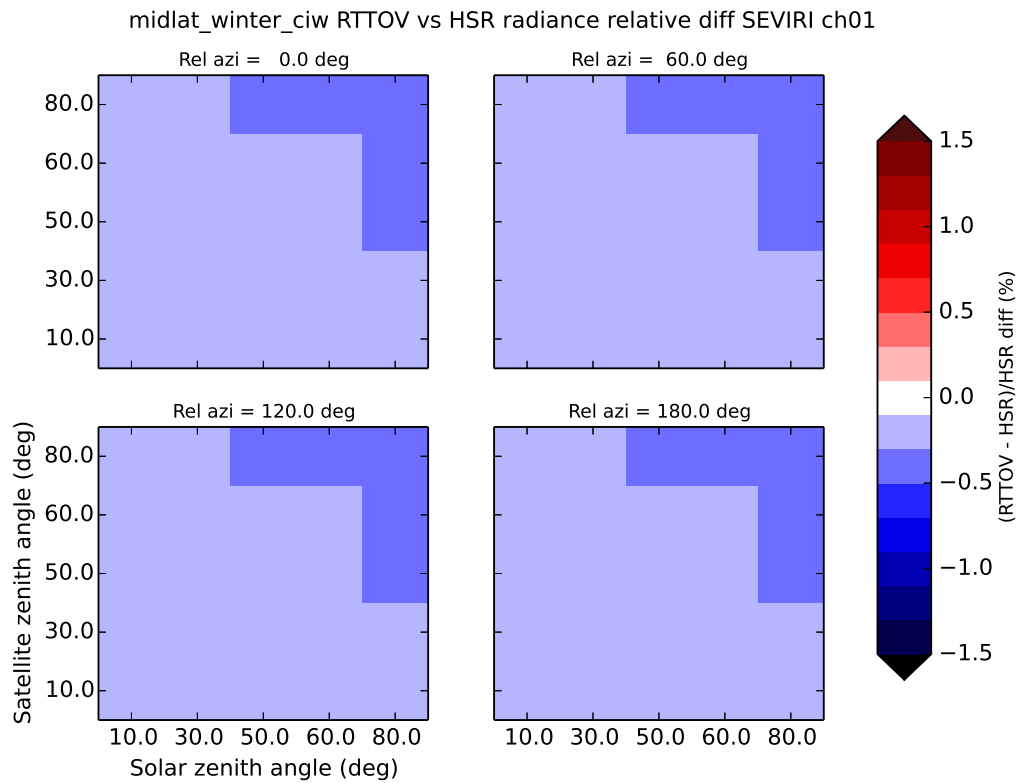


Figure 45: Mid-latitude winter cloud ice water profile, SEVIRI ch01, HSR vs RTTOV using channel-averaged cloud properties

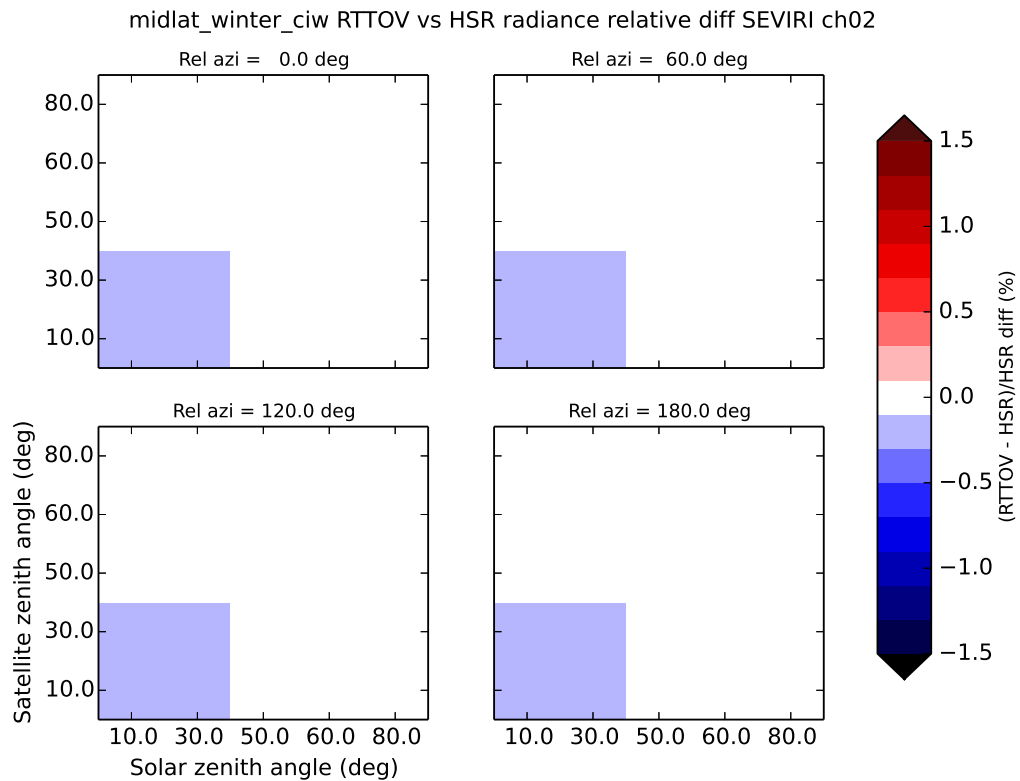


Figure 46: Mid-latitude winter cloud ice water profile, SEVIRI ch02, HSR vs RTTOV using channel-averaged cloud properties



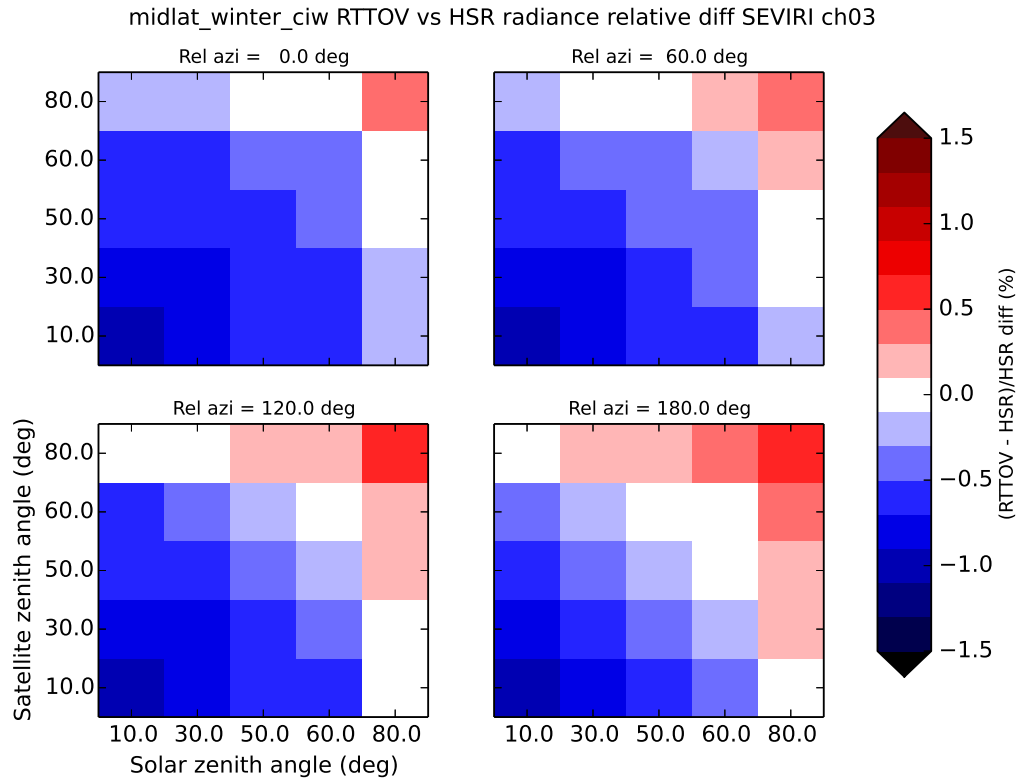


Figure 47: Mid-latitude winter cloud ice water profile, SEVIRI ch03, HSR vs RTTOV using channel-averaged cloud properties

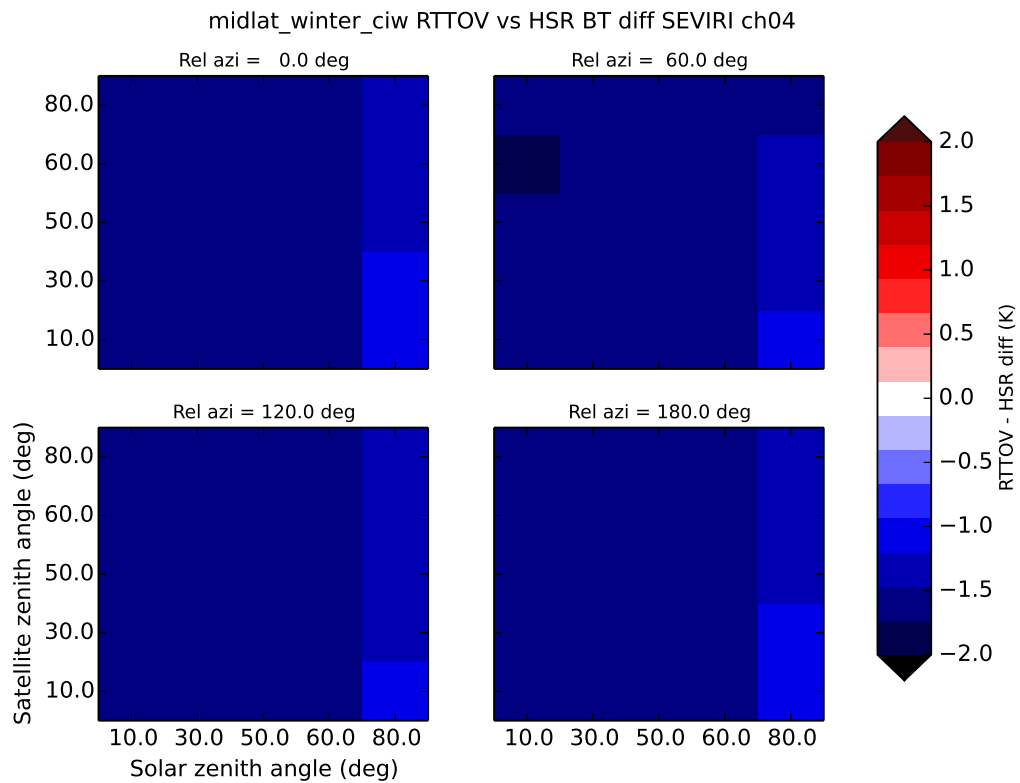


Figure 48: Mid-latitude winter cloud ice water profile, SEVIRI ch04, HSR vs RTTOV using channel-averaged cloud properties

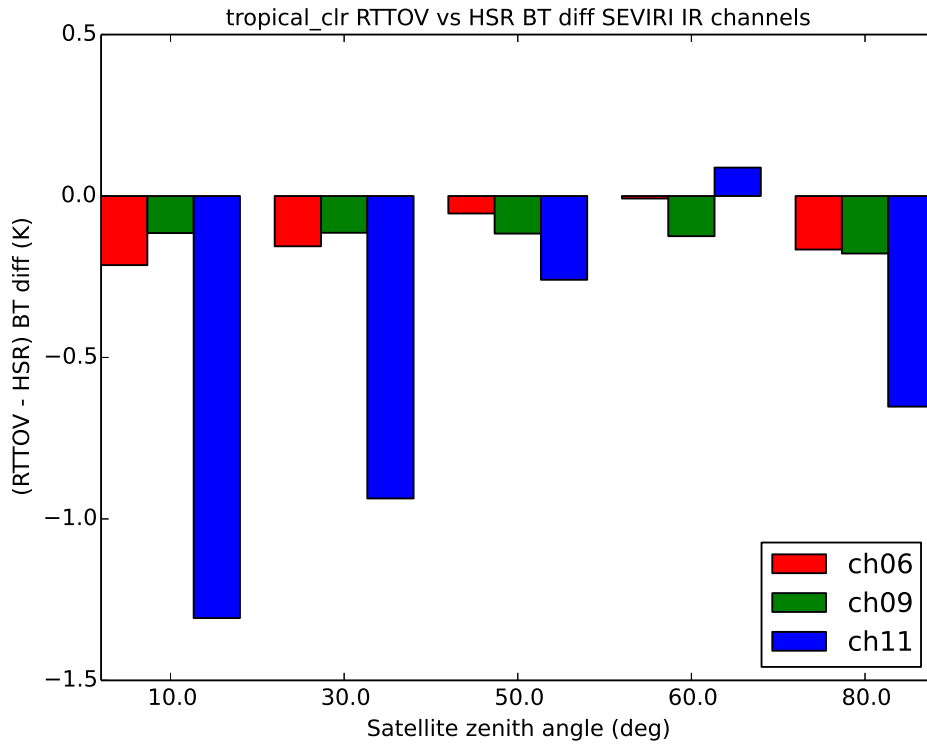


Figure 49: Tropical clear-sky profile, SEVIRI IR channels, HSR vs RTTOV

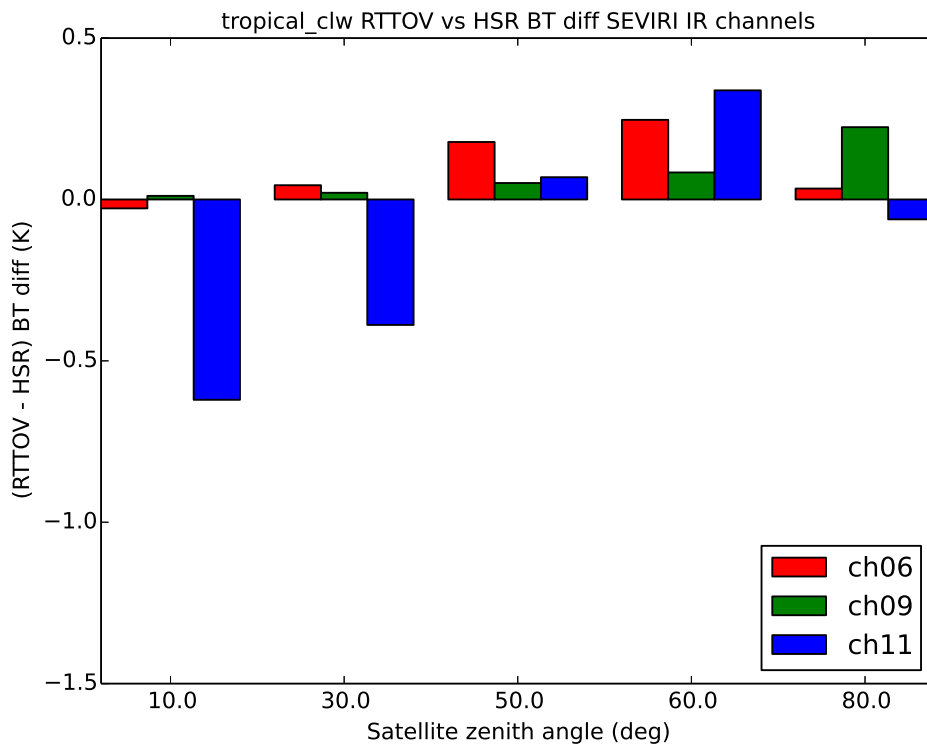


Figure 50: Tropical cloud liquid water profile, SEVIRI IR channels, HSR vs RTTOV

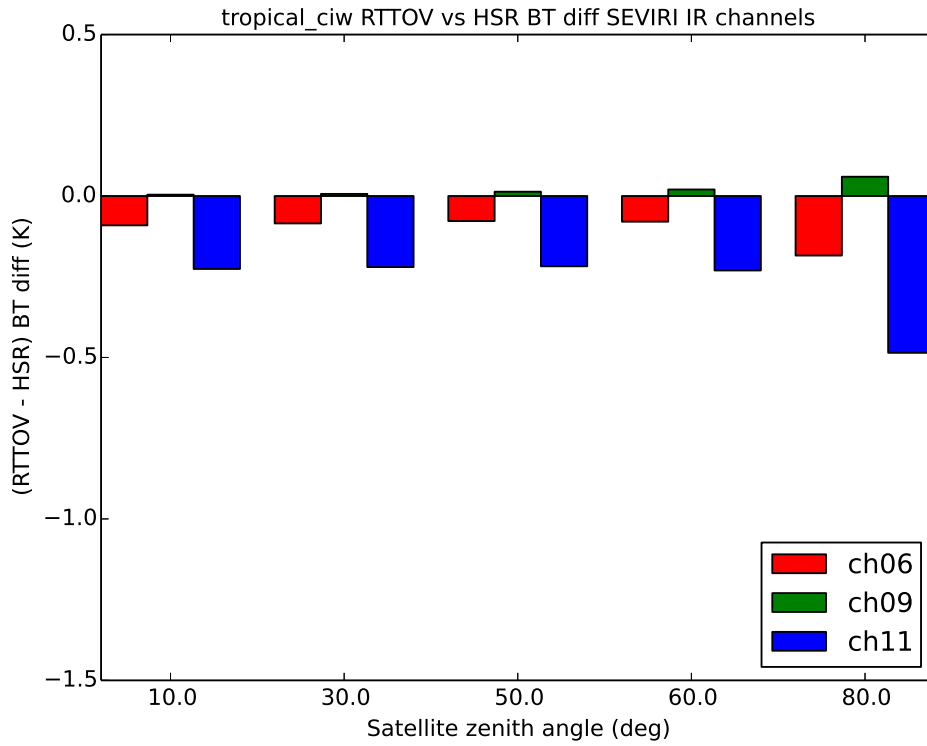


Figure 51: Tropical cloud ice water profile, SEVIRI IR channels, HSR vs RTTOV

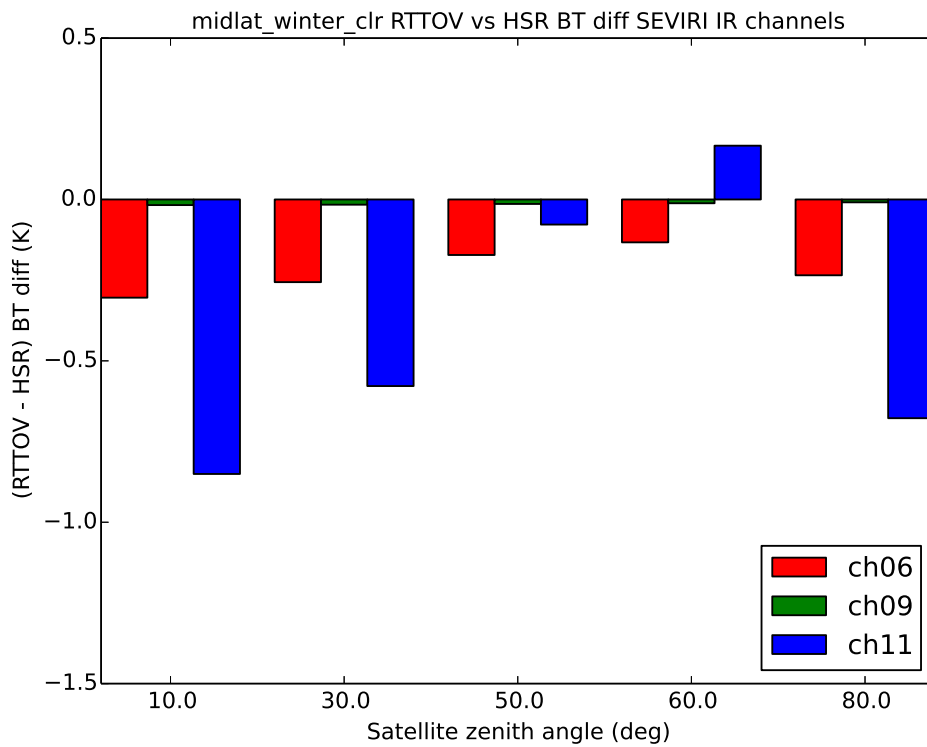


Figure 52: Mid-latitude winter clear-sky profile, SEVIRI IR channels, HSR vs RTTOV

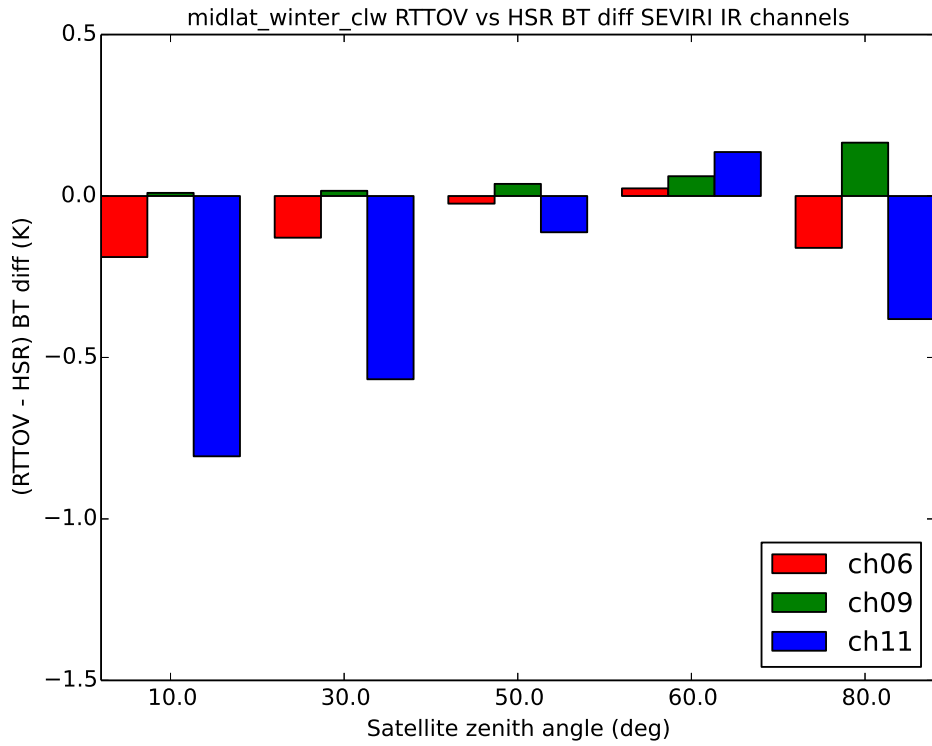


Figure 53: Mid-latitude winter cloud liquid water profile, SEVIRI IR channels, HSR vs RTTOV

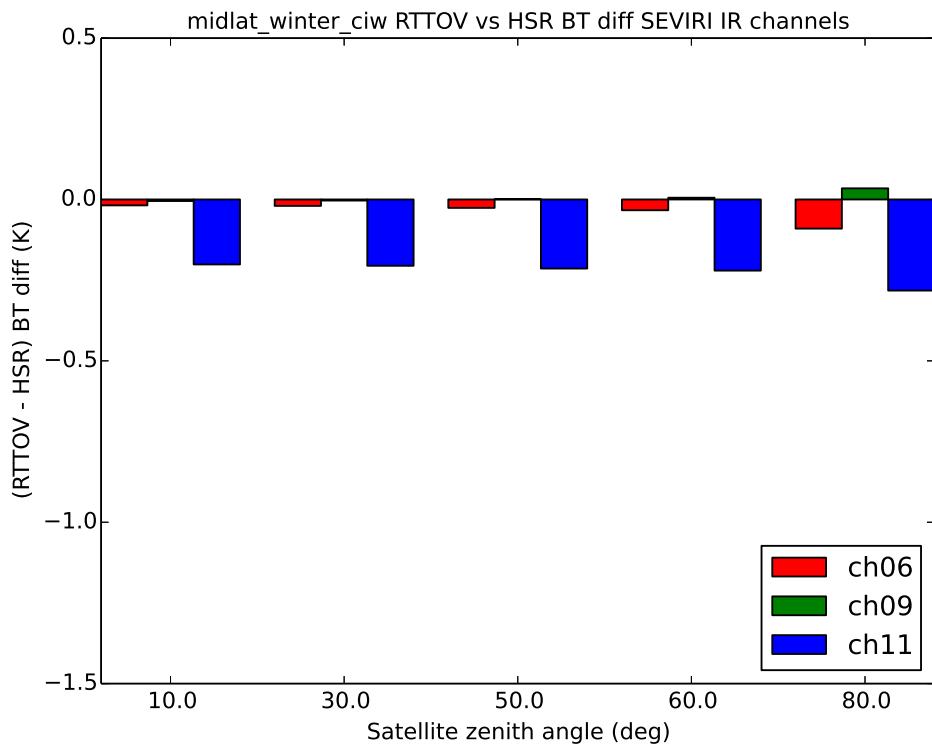


Figure 54: Mid-latitude winter cloud ice water profile, SEVIRI IR channels, HSR vs RTTOV

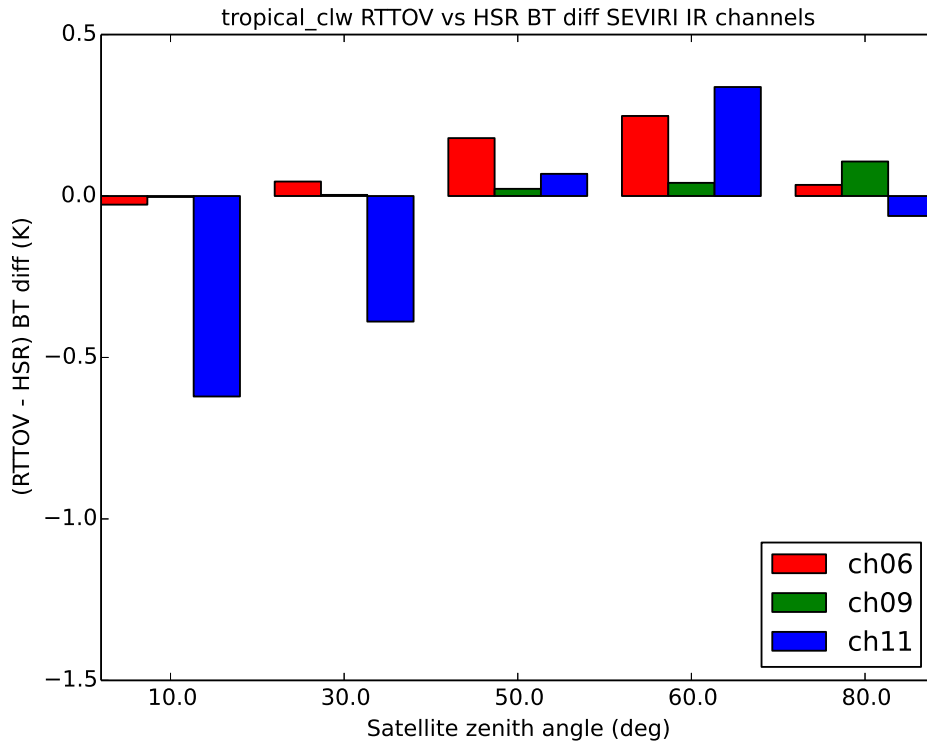


Figure 55: Tropical cloud liquid water profile, SEVIRI IR channels, HSR vs RTTOV with channel-averaged cloud properties

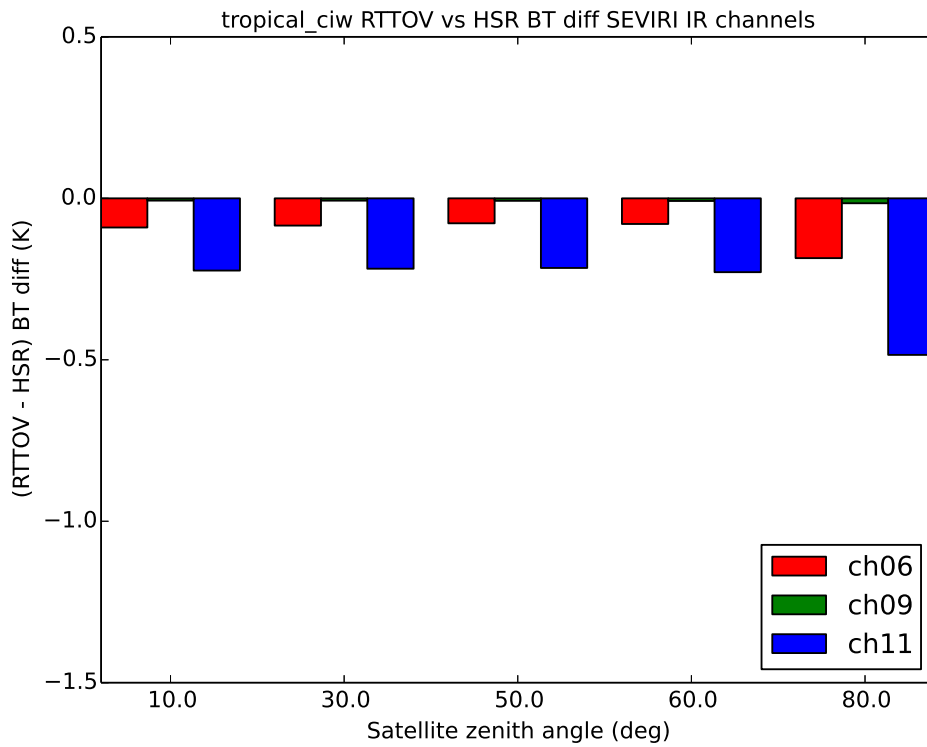


Figure 56: Tropical cloud ice water profile, SEVIRI IR channels, HSR vs RTTOV with channel-averaged cloud properties

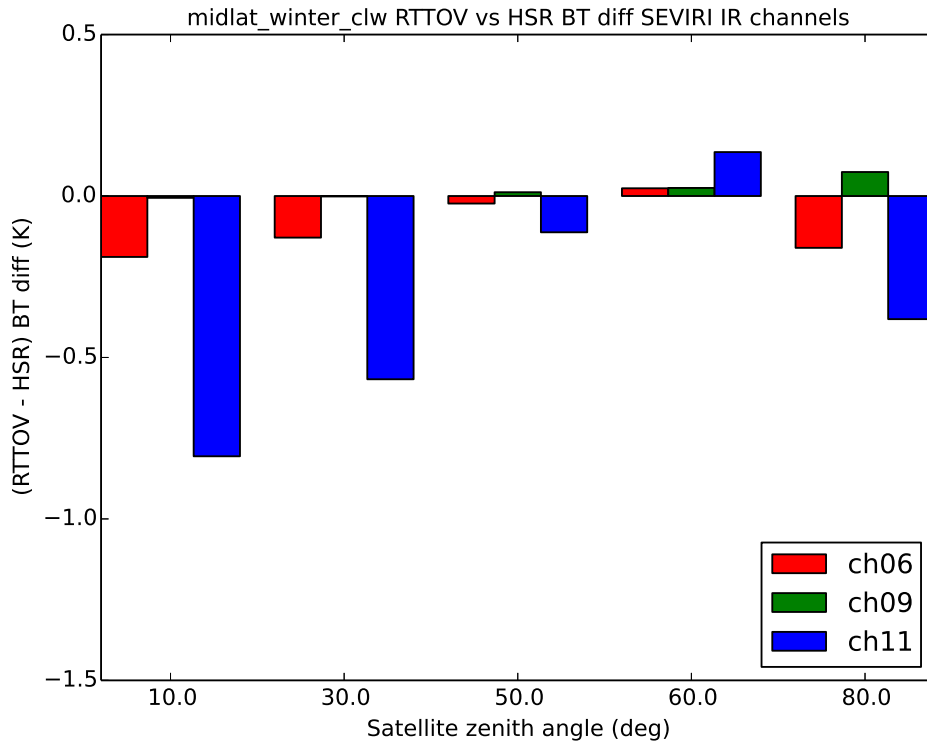


Figure 57: Mid-latitude winter cloud liquid water profile, SEVIRI IR channels, HSR vs RTTOV with channel-averaged cloud properties

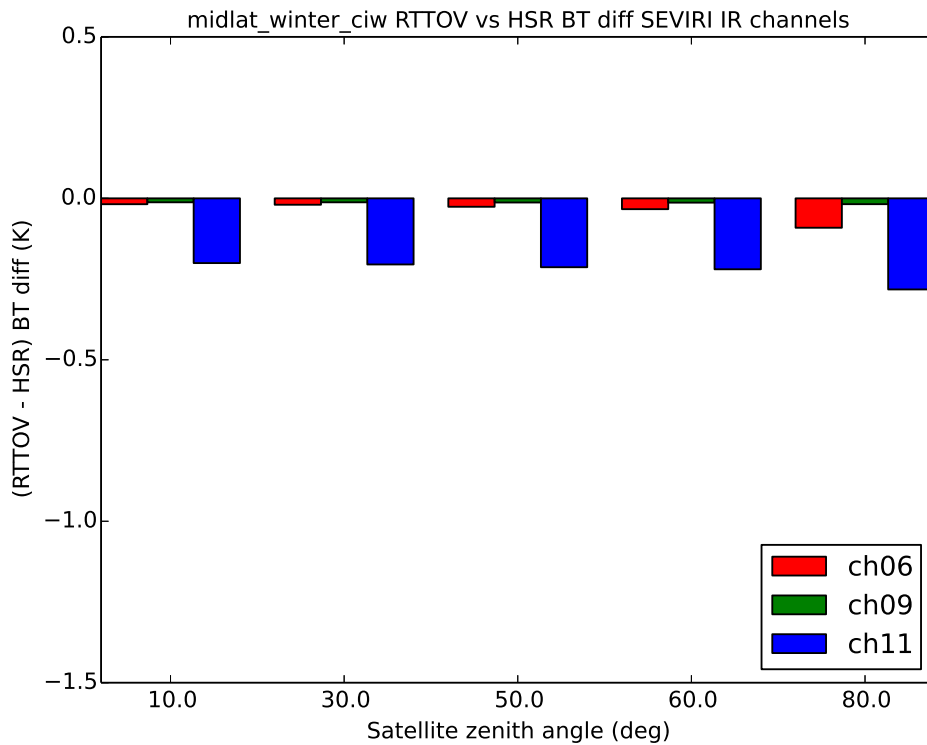


Figure 58: Mid-latitude winter cloud ice water profile, SEVIRI IR channels, HSR vs RTTOV with channel-averaged cloud properties